Petroleum Science 23 (2026) 7321–7337

Contents lists available at ScienceDirect

Petroleum Science

journal homepage: www.keaipublishing.com/en/journals/petroleum-science

Original Paper

Balancing production efficiency and geological risks for safe development of natural gas hydrates depressurization: Effects of bottom-hole pressure and horizontal well placement

Shu-Yang Liu [a,b,c,d], Qi-Zhi Tan [a,b], Chen Fan [a,e], Zhi-Qiang Wang [a,f], Zhi-Yuan Wang [a,b], Jing-Sheng Lu [d], Shu-Xia Li [a,b], Bin Wang [g,*]

[a] School of Petroleum Engineering, China University of Petroleum (East China), Qingdao, 266580, Shandong, China
[b] State Key Laboratory of Deep Oil and Gas, China University of Petroleum (East China), Qingdao, 266580, Shandong, China
[c] Key Laboratory of Gas Hydrate, Ministry of Natural Resources, Qingdao Institute of Marine Geology, Qingdao, 266237, Shandong, China
[d] Guangdong Provincial Key Laboratory of New and Renewable Energy Research and Development, Guangzhou, 510640, Guangdong, China
[e] Drilling Company of CNPC Offshore Engineering Company Limited, Tianjin, 300450, China
[f] State Key Laboratory of Deep Earth Exploration and Imaging, China University of Geosciences, Beijing, 100083, China
[g] Institute of Smart Ocean Science and Engineering, School of Ecology, Environment and Ocean, Guangdong University of Technology, Guangzhou, 510006, Guangdong, China

ARTICLE INFO

Article history:
Received 24 March 2026
Received in revised form
15 May 2026
Accepted 5 July 2026
Available online 11 July 2026

Edited by Meng-Jiao Zhou

Keywords:
Natural gas hydrate
Horizontal-well
Depressurization
Gas production
Geomechanical safety

ABSTRACT

Natural gas hydrates (NGHs) represent a strategic clean energy resource; however, their commercial exploitation is primarily constrained by significant geological risks and low recovery efficiency. In this study, a comprehensive thermal-hydrological-mechanical-chemical (THMC) coupled model, integrated with the Drucker-Prager elastoplastic constitutive criterion, was developed to prioritize the investigation of geomechanical stability under horizontal-well depressurization. The influence of bottom-hole pressure (BHP), vertical positioning of the Producer Horizontal Section (PHS) and underburden thermal convection on formation integrity was systematically evaluated to balance production efficiency and geological risks. While a four-stage gas production evolution was observed, the results emphasize that geomechanical hazards are the primary limiting factor for aggressive drawdown strategies. Although lowering BHP enhances recovery, it exacerbates sediment compaction and threatens seabed stability. Conversely, maintaining BHP above a critical threshold of 4–5 MPa was identified as essential for preserving reservoir integrity. Furthermore, PHS placement was determined to be a critical control for strain localization; a mid-reservoir location was found to optimize the trade-off between decomposition-induced weakening and heat transferred from underlying layers. Geomechanical analysis further revealed that subsidence is most pronounced near the wellbore, with high-risk deformation occurring at the reservoir–overburden interface. These findings underscore the necessity of integrating real-time deformation monitoring with adaptive well designs to mitigate geohazards during the exploitation of deep-sea NGH resources.

© 2026 The Authors. Publishing services by Elsevier B.V. on behalf of KeAi Communications Co. Ltd. This is an open access article under the CC BY-NC-ND license (http://creativecommons.org/licenses/by-nc-nd/4.0/).

1. Introduction

Natural gas hydrates (NGHs) are crystalline compounds in which methane molecules are encapsulated within a lattice of water molecules (Sloan and Koh, 2007). Owing to their enormous methane storage capacity and widespread occurrence, NGHs are increasingly recognized as a strategic alternative energy resource (Chong et al., 2016). Estimates indicate that the global methane reserves in hydrate form may be about twice the combined proven reserves of conventional fossil fuels, highlighting their strategic significance for future energy supply (Gajanayake et al., 2023; Wang et al., 2018). Given that natural gas hydrates (NGHs) are recognized as a cleaner energy source (Kvenvolden, 1988), the

* Corresponding author.
E-mail address: binwang@gdut.edu.cn (B. Wang).
Peer review under the responsibility of China University of Petroleum (Beijing).

https://doi.org/10.1016/j.petsci.2026.07.008
1995-8226/© 2026 The Authors. Publishing services by Elsevier B.V. on behalf of KeAi Communications Co. Ltd. This is an open access article under the CC BY-NC-ND license (http://creativecommons.org/licenses/by-nc-nd/4.0/).

primary focus of energy research has transitioned from resource assessment to addressing the complex technical challenges of their development (Yang et al., 2024).

In nature, NGH stability is maintained only under the high-pressure and low-temperature conditions characteristic of terrestrial permafrost and deep-sea continental margins (Skarke et al., 2014; Wang et al., 2025). In marine environments, NGHs are predominantly distributed along continental shelves and slopes, typically at water depths exceeding 500 m (Makogon et al., 2007). Over 95% of global NGH reserves are estimated to reside in these deep-sea sediments (Max and Johnson, 2018). Despite this abundance, commercial viability is fundamentally hindered by significant technical and geomechanical safety challenges (Li et al., 2025; Yuan et al., 2025). Several countries, including the United States, Japan, and China, have conducted field production tests to evaluate the feasibility of NGH exploitation (Kurihara et al. 2010; Li et al., 2018, Moridis et al., 2004, ; Yamamoto et al., 2014 Yamamoto et al., 2019). A notable example is the second production test in the Shenhu area of the South China Sea, which demonstrated that horizontal-well depressurization significantly enhances recovery rates compared to vertical configurations (Ye et al., 2020; Yin et al., 2022), but it simultaneously amplifies the geological risks inherent to hydrate-bearing formations. Furthermore, to optimize production efficiency in complex geological settings, multilateral horizontal wells have been extensively investigated (Jin et al., 2023; Mao et al., 2023; Wan et al., 2024). Although such configurations significantly expand the decomposition zone and accelerate gas recovery, they inevitably provoke more drastic localized pressure drawdowns and effective stress variations. This exacerbated geomechanical response substantially elevates the risk of severe reservoir subsidence and structural failure (Ye et al., 2024).

The exploitation of NGH-bearing reservoirs is complicated by the fact that they often consist of weakly cemented, fine-grained sediments, such as muddy silt (Hyodo et al., 2017; Lei and Santamarina, 2018). Extensive depressurization in these unstable formations can trigger seabed subsidence and submarine landslides, posing threats to offshore infrastructure and marine ecosystems (Li et al., 2021b, Song et al., 2024). For instance, the transient excess pore pressure generated during marine gas hydrate dissociation has been demonstrated to severely compromise both the long- and short-term dynamic stability of submarine slopes (Song et al., 2023). Therefore, preventing geohazards has become a paramount concern for NGH exploitation, requiring a balance between extraction efficiency and geomechanical stability. Current research efforts are increasingly focused on developing safer extraction techniques that can mitigate these risks while maintaining economic viability (Tiong et al., 2025; Yang et al., 2017).

The inherent risks of depressurization-based exploitation have been confirmed by previous field trials. For instance, substantial seabed subsidence was observed during Japan's first production test in the Nankai Trough following NGH decomposition (Akaki et al., 2016). This phenomenon is primarily driven by pore pressure reduction, which increases effective stress on the sediment framework, leading to compaction and structural deformation (Yoneda et al., 2018). Furthermore, NGHs serve as a cementing agent that enhances the mechanical stability of marine sediments. Upon dissociation, the loss of this binding effect significantly weakens the sediment's mechanical strength, exacerbating strata deformation (Wu et al., 2020). These combined effects—pore pressure depletion and reduced cohesion—can destabilize submarine slopes, potentially triggering catastrophic secondary disasters such as large-scale submarine landslides or even tsunamis (Maslin et al., 2004).

To quantify these risks, the mechanical properties of NGH-bearing sediments must be accurately characterized. Yoneda et al. (2015) conducted triaxial shear tests on intact core samples from the Nankai Trough, revealing that the yield behavior of NGH-bearing sediments follows the Mohr–Coulomb failure criterion. Their work demonstrated a linear correlation between hydrate saturation and Young's modulus, highlighting the stiffening effect of hydrates on sediment structure. Dong et al. (2020) performed systematic triaxial tests on laboratory-synthesized hydrate-bearing cores and fitted the triaxial test results using the Mohr–Coulomb, Drucker–Prager, and Lade–Duncan criteria, finding that the first two criteria provided good agreement with their experimental results. They also observed that both the internal friction angle and cohesion of NGH-bearing sediments have a linear relationship with hydrate saturation. Zhang et al. (2015) used tetrahydrofuran to form hydrate in sediment cores from the South China Sea and demonstrated that the Drucker–Prager criterion effectively captured the shear strength behavior of these synthetic hydrate-bearing sediments. Wang et al. (2021) developed a statistical damage constitutive model that accurately describes both the strength characteristics and softening behavior of NGH-bearing sediments; however, its high computational cost limits its applicability. Ye et al. (2026) elucidated the multi-stage gas production mechanisms inherent to Class I, II, and III hydrate reservoirs utilizing a novel thermally-segmented rotatable reactor. Their experimental results indicated that low hydrate saturation enhanced permeability and thus accelerated gas production. These studies collectively demonstrate that hydrate saturation significantly influences sediment mechanical properties. In addition, recent laboratory and modeling studies have shown that effective stress and hydrate dissociation jointly control permeability evolution during depressurization, directly impacting deformation and production behavior (Wang et al., 2023; Wu et al., 2022).

Field-scale numerical simulation serves as a critical tool for optimizing the economic viability and safety of NGH exploitation (Liu et al., 2022; Sun et al., 2019). Recent advancements have enabled the evaluation of gas production performance using thermal–hydrological–chemical (THC) coupling approaches. For instance, Dong et al. (2023) clarified the thermodynamic non-equilibrium mechanisms during long-period depressurization, informing pressure-management strategies. It is also underscored in Gong et al. (2025) that production efficiency and thermo-hydrodynamic driving forces depend sensitively on pressure strategies and reservoir conditions, with implications for stability management (Cui et al., 2024). However, the integration of comprehensive mechanical effects for geological risks assessment remains underdeveloped.

To tackle this issue, Matsuda et al. (2016) conducted pioneering work analyzing reservoir subsidence under depressurization, demonstrating the influence of Young's modulus on deformation patterns. Li et al. (2021a) investigated vertical wellbore deformation, emphasizing the combined effects of Young's modulus and bottom-hole pressure on structural integrity. Lee et al. (2021) proposed a cyclic depressurization method to enhance production while controlling subsidence. Their results indicated that frequent pressure oscillations from well opening/closing cycles could induce geological fatigue, potentially leading to long-term formation instability. Jin et al. (2018) extended the TOUGH + Hydrate simulator to incorporate mechanical modeling, enabling analysis of stress evolution in sediments during horizontal-well depressurization. More recently, the Thermo-Hydro-Mechanical-Chemical (THMC) coupled framework has been adopted to evaluate the complex multi-physical processes of field-scale NGH exploitation in the South China Sea. Ye et al. (2025a) utilized a THMC model to evaluate gas production through depressurization

coupled with thermal stimulation, revealing that the hydro-lock effect in muddy silt reservoirs severely restricts gas permeation, a limitation that can be partially mitigated through hydraulic fracturing. Furthermore, Ye et al. (2025b) extended the THMC framework to simulate hydrate-based CO_2 sequestration in post-exploitation reservoirs, where the formation of mixed CO_2-CH_4 hydrates was demonstrated to facilitate geological restoration and strata support.

Despite these developments, previous studies on thermal–hydrological–mechanical–chemical (THMC) coupling remain inadequate for assessing long-term geological risks associated with horizontal-well depressurization. A critical limitation lies in the suboptimal integration of sediment mechanical behavior, primarily resulting from the inefficient utilization of laboratory-derived triaxial shear test data. While prior studies have provided profound insights into fluid migration and post-exploitation remediation, the structural safety of the primary extraction phase remains unresolved. Consequently, the dynamic trade-off between heat transfer efficiency (specifically, the upward intrusion of relatively warm underburden water) and geomechanical stability—particularly under varying bottom-hole pressures (BHPs) and vertical placements of the producer horizontal section (PHS)—has not been systematically quantified.

To address these deficiencies, this study introduces a THMC-coupled numerical simulation framework, incorporating a Drucker–Prager (DP) elastoplastic constitutive model, for balancing production efficiency and geological risks during NGH depressurization. Selected for its computational robustness and efficacy in capturing complex sediment deformation, the DP model is rigorously parameterized using experimental shear test data to accurately represent sediment deformation. Based on this, this study systematically quantifies the spatiotemporal evolution of geohazards driven by the dynamic interplay between wellbore operational parameters and underburden thermal convection. By evaluating both BHP and vertical PHS placement, this research provides critical insights for establishing safer exploitation protocols that maximize heat transfer efficiency while prioritizing long-term geomechanical stability.

2. Methodology

2.1. Mathematical model

Prior to model development, the following assumptions are made: (1) Only gas–liquid two-phase flow is considered during the exploitation of NGH-bearing reservoirs, and the flow obeys Darcy's law. (2) The NGH-bearing reservoir is assumed to be homogeneous, with parameters such as porosity and saturation uniformly distributed at the same horizontal position. (3) Gas dissolution and diffusion in the liquid phase are neglected.

2.1.1. Mass conservation equations

The mass conservation equations for each component are given as follows (Fu et al., 2025; Xue et al., 2023).

(1) Water phase

$$\frac{\partial}{\partial t}(\rho_w \phi S_w) = -\nabla(\rho_w v_w) - q_w + m_w \tag{1}$$

(2) Gas phase

$$\frac{\partial}{\partial t}(\rho_g \phi S_g) = -\nabla(\rho_g v_g) - q_g + m_g \tag{2}$$

(3) Hydrate phase

$$-\frac{\partial}{\partial t}(\rho_h \phi S_h) = m_w + m_g \tag{3}$$

where ρ_w, ρ_g and ρ_h are densities of water, gas and hydrate, respectively, kg·m^{-3}; S_w, S_g and S_h are their respective saturations; q_w and q_g are the production rates of water and gas, m^3·s^{-1}; m_s and m_g are the reaction rates of water and gas, kg·s^{-1}; v_w and v_g are the flow velocities of water and gas, m^3·s^{-1}; and ϕ is porosity.

2.1.2. Energy conservation equation

The energy conservation equation is given as follows (Qiu et al., 2023, Xue et al., 2023):

$$-\frac{\partial}{\partial t}\left(C_{eff}T\right) = \nabla\left(\lambda_{eff}\nabla T\right) + \left[\left(v_w\rho_w C_w + v_g\rho_g C_g\right)T\right] - n_h\Delta H_h + q_w C_w T + q_g C_g T \tag{4}$$

$$C_{eff} = (1-\phi)\rho_r C_r + \phi\left(S_w\rho_w C_w + S_g\rho_g C_g + S_h\rho_h C_h\right) \tag{5}$$

$$\lambda_{eff} = (1-\phi)\lambda_r + \phi\left(S_w\lambda_w + S_g\lambda_g + S_h\lambda_h\right) \tag{6}$$

where T is absolute temperature, K; ρ_r is density of the rock, kg·m^{-3}; C_r, C_w, C_g and C_h are the specific heat capacity of the rock, water, gas, and hydrate, respectively, J·kg^{-1}·K^{-1}; λ_r, λ_w, λ_g and λ_h are their heat conductivities, W·kg^{-1}·K^{-1}; n_h is the reaction rate of hydrate, mol·m^{-3}·s^{-1}; and ΔH_h is latent heat absorbed during hydrate decomposition per unit volume, J·mol^{-1}.

2.1.3. Reaction kinetics equation

The reaction kinetics equation is given as follows (Fu et al., 2025):

$$-\frac{\partial c_h}{\partial t} = k^0\phi^2 A_{hs} S_w S_h p_e\left(1-\frac{p_g}{p_e}\right)\cdot\exp\left(-\frac{E}{RT}\right) \tag{7}$$

where k^0 is the intrinsic reaction rate constant, mol·m^{-2}·Pa^{-1}·s^{-1}; A_{hs} is the specific surface area of hydrate particles, m^{-1}; p_e is the gas hydrate equilibrium pressure, Pa, and varies with temperature; p_g is the liquid pressure, Pa. At a given temperature, hydrate decomposition occurs when $p_g < p_e$, while hydrate formation takes place when $p_g > p_e$.

2.1.4. Rock mechanics constitutive model

The yield failure behavior of NGH-bearing sediments conforms to the DP yield criterion. The criterion is expressed as (Dong et al., 2020; Masui et al. 2007; Yoneda et al., 2015):

$$\begin{cases} \sqrt{J_2} = A + BI \\ J_2 = \dfrac{1}{6}\left[(\sigma_1-\sigma_2)^2 + (\sigma_1-\sigma_3)^2 + (\sigma_2-\sigma_3)^2\right] \\ I_1 = \sigma_1 + \sigma_2 + \sigma_3 \\ A = \dfrac{6c\cdot\cos\phi}{\sqrt{3}(3-\sin\phi)} \\ B = \dfrac{2\cdot\sin\phi}{\sqrt{3}(3-\sin\phi)} \end{cases} \tag{8}$$

The internal friction angle, cohesion and Young's modulus of the sediments are assumed to increase linearly with hydrate saturation, as expressed as (Dong et al., 2020; Yoneda et al., 2015):

$$\begin{cases} \phi(S_h) = \phi_0 + \phi_h S_h \\ c(S_h) = c_0 + c_h S_h \end{cases} \tag{9}$$

where Φ_0 and Φ_h are the internal friction angles of the sediment matrix and hydrate, respectively, °; c_0 and c_h are the corresponding cohesion values, Pa; and σ_1 and σ_3 are the maximum and minimum principal stresses, Pa. Under triaxial shear test conditions, $\sigma_1 = \sigma_3$.

By substituting c and Φ in Eq. (8) with the expressions in Eq. (9), the relationship between the maximum deviatoric stress p_{max} (in Pa) of the sediment and hydrate saturation can be obtained (Dong et al., 2022):

$$p_{max} = (\sigma_1 - \sigma_3)_{max} = \frac{2c(S_h)\cdot\cos\phi(S_h) + 2\sigma_3\cdot\sin\phi(S_h)}{1-\sin\phi(S_h)} \tag{10}$$

The deviatoric stress p^{50} is calculated as half of p_{max}, which is then used to determine the corresponding axial strain ε^{50} based on the stress–strain curve obtained from triaxial shear tests. The secant modulus E^{50} (in Pa) at various hydrate saturations S_h is calculated by (Dong et al., 2022):

$$E^{50} = p^{50} \Big/ \varepsilon^{50} \tag{11}$$

The linear relationship between secant modulus and hydrate saturation is expressed as (Dong et al., 2022):

$$E^{50}(S_h) = E_0^{50} + E_h^{50} S_h \tag{12}$$

where E_0^{50} and E_h^{50} are the secant moduli of the sediment matrix and hydrate, respectively (in Pa).

This elastoplastic constitutive model, based on the DP yield criterion and calibrated with triaxial shear test data, is integrated into the THMC simulation framework to compute sediment deformation in the linear elastic regime prior to yield failure. The model is both computationally efficient and adaptable, enabling dynamic adjustment based on changes in NGH saturation during hydrate exploitation.

2.1.5. Fluid viscosity model

To precisely characterize fluid transport within the hydrate-bearing sediments, the temperature-dependent flow behaviors of the water and gas phases are formulated as (Reid et al., 1959):

$$\mu_w = \alpha_w \cdot \exp\left(\frac{\beta_w}{T}\right) \tag{13}$$

$$\mu_g = \alpha_g + \beta_g \cdot T \tag{14}$$

where α_w and β_w are water viscosity coefficients with the values of 4.74×10^{-3} cp and 1515.70 K, respectively, while α_g and β_g are gas viscosity coefficients with the values of 1.36×10^{-2} cp and 3.8×10^{-5} cp/K, individually.

2.2. Model construction

As shown in Fig. 1(a), a homogeneous model of the NGH-bearing reservoir was constructed based on field data from the Nankai Trough pilot production test (Konno et al., 2017). The model domain extends 1000 × 1000 × 390 m in the x, y, and z directions, and is divided into 85 × 85 × 103 grid cells. Vertically, the model comprises three layers: an overburden layer (z = 110–390 m), an NGH-bearing reservoir (z = 50–110 m), and an underburden layer (z = 0–50 m). The grid thickness is set to 2 m from the model bottom to 50 m above the reservoir, and 10 m elsewhere horizontally, cell size varies from 2 × 2 m at the center and 32 × 32 m at the corners. The initial sediment subsidence is assumed to be zero, and the model bottom is defined as a no-displacement boundary. The overburden and underburden layers, composed of muddy silt sediments without NGHs, have horizontal permeabilities of 1×10^{-3} μm^2 and 100×10^{-3} μm^2, respectively. According to the measured permeability ranges (0.01–10 mD) (Konno et al., 2017) and the classical permeability anisotropy range (0.1–1) (Feng et al., 2019; Zhu et al., 2020) of the Nankai Trough, The NGH-bearing reservoir has an initial permeability of 5×10^{-3} μm^2 and the ratio of vertical to horizontal

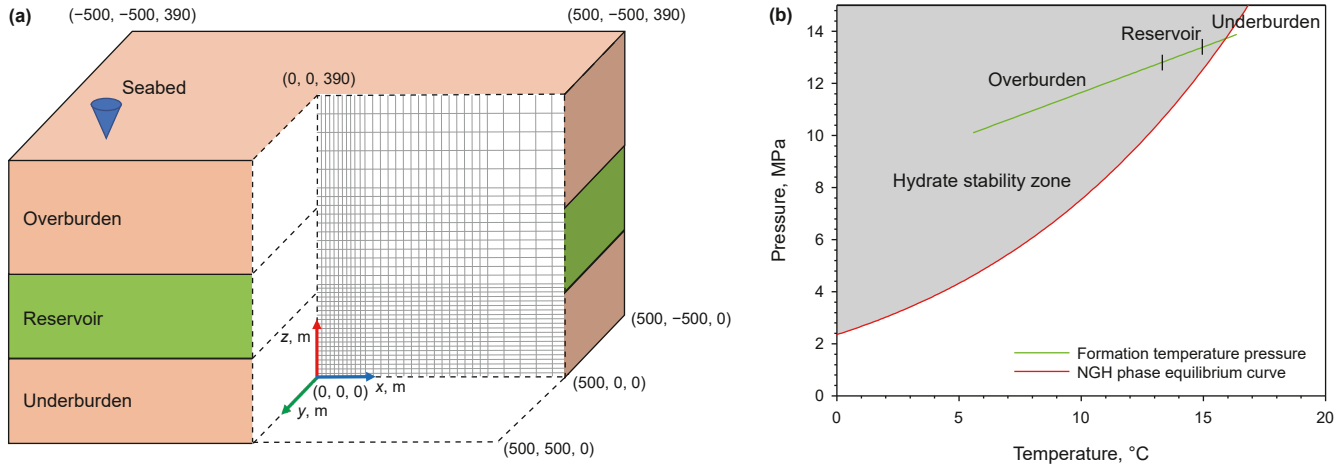


Fig. 1. **(a)** Schematic diagram of the NGH-bearing reservoir model, and **(b)** temperature-pressure profile of the modelled sediments and NGH equilibrium curve.

Table 1
Main parameters of the NGH-bearing reservoir model.

Parameter	Value	Parameter	Value
Reservoir dimensions	1000 × 1000 × 390 m	ϕ_0	34.6°
Overburden thickness	280 m	ϕ_h	34.6°
Reservoir thickness	60 m	c_0	0 Pa
Underburden thickness	50 m	c_h	8250 Pa
Overburden porosity	0.4	E_0^{50}	2.53×10^6 Pa
Reservoir porosity	0.4	E_h^{50}	0.36×10^6 Pa
Underburden porosity	0.4	Intrinsic permeability of overburden	$K_h = 1 \times 10^{-3}$ μm^2
Overburden water saturation	1		$K_v = 0.8 \times 10^{-3}$ μm^2
Reservoir water saturation	0.29	Intrinsic permeability of NGH-bearing reservoir	$K_h = 5 \times 10^{-3}$ μm^2
Reservoir hydrate saturation	0.71		$K_v = 4 \times 10^{-3}$ μm^2
Underburden water saturation	1	Intrinsic permeability of underburden	$K_h = 100 \times 10^{-3}$ μm^2
Rock thermal conductivity	1.74 W m^{-1} K^{-1}		$K_v = 80 \times 10^{-3}$ μm^2
Hydrate thermal conductivity	0.6 W m^{-1} K^{-1}	Initial seabed temperature	5 °C
Water thermal conductivity	0.7 W m^{-1} K^{-1}	Temperature gradient	0.03 °C·m^{-1}
Gas thermal conductivity	0.03 W m^{-1} K^{-1}	Initial seabed pressure	1×10^4 kPa
Poisson's ratio	0.3	Pressure gradient	9.8 kPa m^{-1}

permeability is set as 0.8. The initial temperature and pressure profiles from overburden to underburden are shown in Fig. 1(b), and the NGH-bearing layer satisfies the thermodynamic stability conditions for NGH occurrence. The main parameters of the reservoir model are summarized in Table 1.

2.3. Model validation

The feasibility of the constructed model is validated by comparing the simulation results with the data from the Nankai Trough pilot production test (Konno et al., 2017). A vertical production well penetrated 38 m into the hydrate-bearing layer and perforated from $z = 72$ m to $z = 110$ m at the center of the reservoir model. The well operated under a production pressure of 4 MPa. Fig. 2 presents the simulated gas and water production rates over a 7-day period. The simulated gas production rate closely matches the field measurements starting from day three. However, the simulated water production rate exceeds that observed in the field test. This discrepancy may be attributed to two factors: (1) During the initial days of the field production, some NGHs near the wellbore may have already decomposed due to wellbore operations before the formal start of production, which was not accounted in the simulation. (2) Downhole water separation devices used in the field were not accounted for in the reservoir model, leading to overestimated water production. Similar overestimations have been reported in previous studies by Sun et al. (2016) and Zhu et al. (2020), indicating that this is a recognized and unsolved issue in current modeling approaches. Therefore, the validated model in this study is considered reliable and suitable for simulating the depressurization exploitation of NGH-bearing reservoirs.

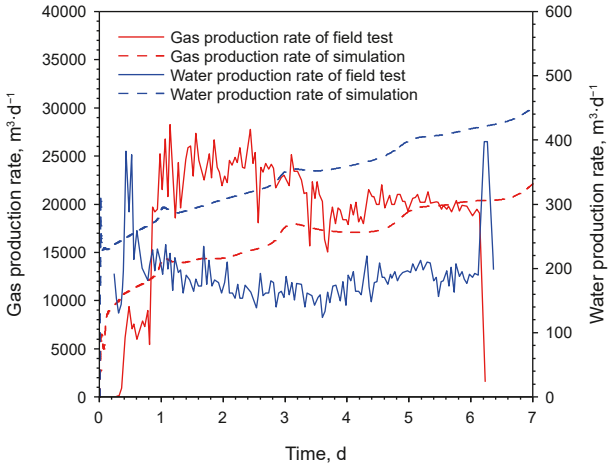


Fig. 2. Comparison of simulated gas and water production rates with field measurements.

3. Results and discussion

3.1. Basic characteristics of horizontal-well depressurization of NGH-bearing reservoirs

Horizontal-well depressurization has emerged as a pivotal technique for the commercial exploitation of NGH resources (Yin et al., 2022). In this section, a base-case model with a horizontal production well was established to investigate depressurization-based NGH exploitation. The well design features: (1) a non-perforated vertical section for structural integrity, and (2) a fully perforated producer horizontal section (PHS) strategically positioned 20 m above the reservoir's bottom boundary ($z = 70$ m). The production system operates at a constant bottom-hole pressure (BHP) of 4 MPa, with the simulation extending over a 1000-day period to capture both short-term production dynamics and long-term reservoir response. This configuration represented a balanced approach between production efficiency and geological stability, enabling comprehensive evaluation of key performance indicators including gas production rates, NGH decomposition patterns, and formation stability throughout the exploitation process.

3.1.1. Gas and water production characteristics

Fig. 3 shows the gas and water production rates of the base case over a 1000-day simulation period, and the corresponding cumulative production. Based on the variation of gas production rate, the production process can be divided into four stages. Stage A (Rapid rise): The gas production rate quickly increased from zero to a peak of 2777 m^3 d^{-1} by day 59. Stage B (Sharp decline): The rate sharply decreased to 1876 m^3 d^{-1} by day 150. Stage C (Gradual decline): A slow decline was observed, with the rate falling to 570 m^3 d^{-1} by day 542. Stage D (Low production): From day 542 to day 1000, the gas production rate slightly increased to 598 m^3 d^{-1} by day 652, followed by a decline to 239 m^3 d^{-1} at the end of the simulation. The water production rate initially rose sharply, reaching a peak of 42 m^3 d^{-1} in Stage A, followed by a continuous

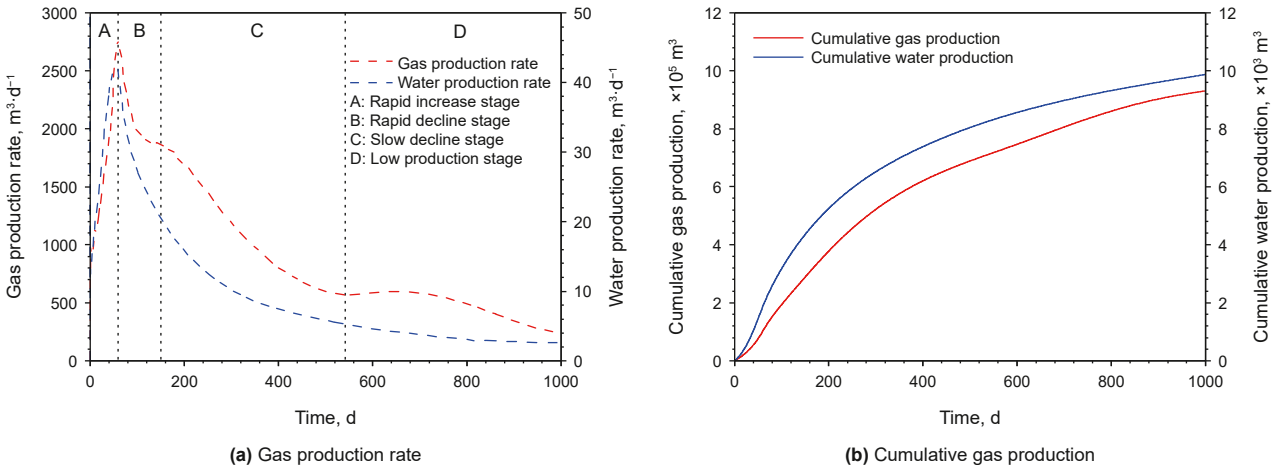


Fig. 3. **(a)** Gas and water production rates and **(b)** cumulative gas and water production under the base case scenario.

decline during Stages B and C, and eventually stabilizing at 2.6 m^3 d^{-1} in Stage D. Over the 1000-day production period, the cumulative gas and water productions reached 9.31 $\times$ 10^5 m^3 and 9875.4 m^3, respectively, corresponding to a cumulative gas-to-water ratio of 94.27.

To further analyze the production behaviors, the evolution of sediment properties across different stages was investigated. Fig. 4 shows the spatiotemporal distributions of temperature, pressure, hydrate saturation, and gas saturation within the reservoir. In Stage A (day 50), as shown in Fig. 4(b), gas production triggers obvious pressure drawdown around the horizontal wells, driving rapid NGH decomposition at the position of $x = -21.91$ to 21.91 m and z = 50.00 to 79.20 m (Fig. 4(c)). The pressure reduction extended into the underburden layer, causing upward water inflow from the underburden that carried additional heat into the NGH-bearing reservoir and further accelerated NGH decomposition (Fig. 4(a)). The decomposition of NGHs near the gas-producing well significantly increased the permeability in these areas, promoting efficient pressure transmission and leading to sharp increases in both gas and water production. These numerical observations are highly consistent with recent experimental findings (Ye et al., 2026), which demonstrated that the pressure drops derived from the production of free gas facilitates upward thermal convection, which effectively compensates for the latent heat consumed during natural gas hydrate (NGH) dissociation. However, experimental investigations typically employ the rigid boundary conditions in high-pressure reactors, which inherently suppress geomechanical deformation and maintain static sediment skeletal structures (Shi et al., 2024; Yao et al., 2024; Ye et al. 2026). Conversely, the field-scale THMC model integrated with the

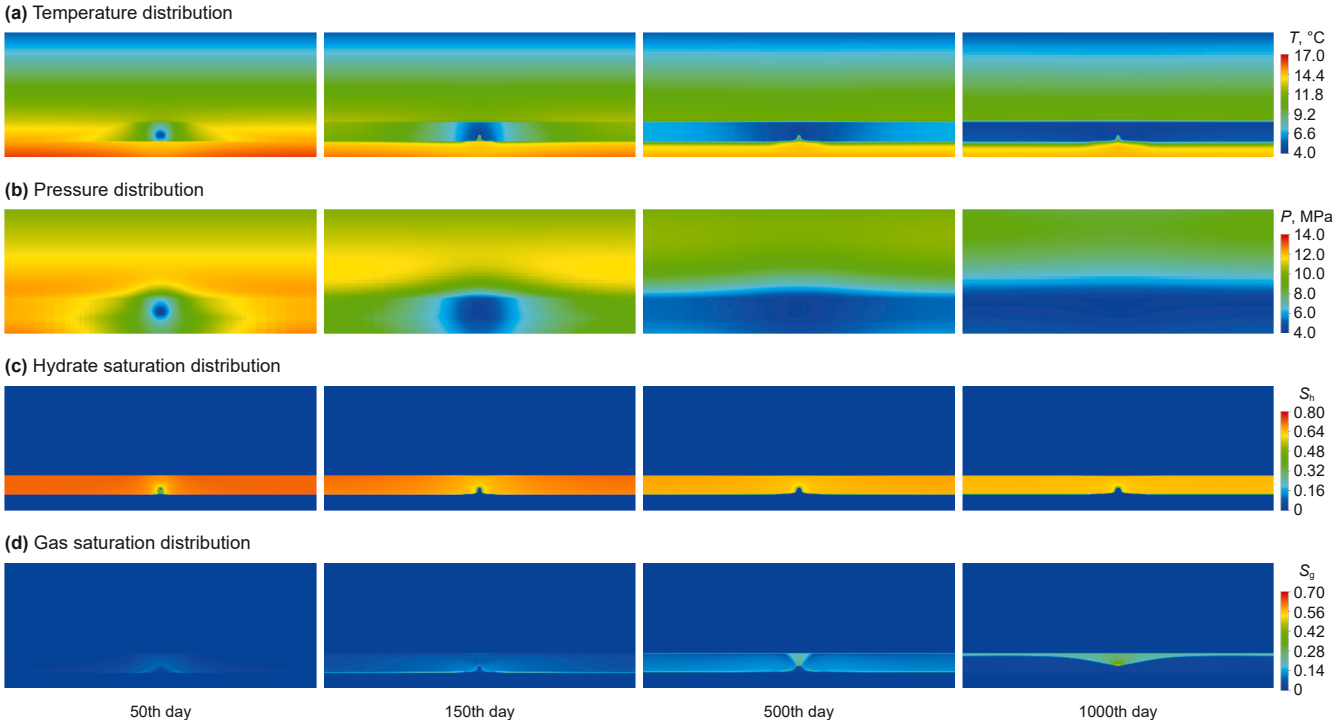


Fig. 4. Simulated distributions of **(a)** temperature, **(b)** pressure, **(c)** hydrate saturation, and **(d)** gas saturation in the base case.

Drucker-Prager elastoplastic criterion reveals that depressurization-induced effective stress variations lead to dynamic porosity reduction, sediment compaction, and potential structural failure, which underscores the necessity of incorporating coupled elastoplastic geomechanical evaluations to accurately predict long-term production efficiency and geohazard risks.

In Stage B (day 150), Fig. 4(b) reveals that the inlet pressure had propagated throughout the NGH-bearing reservoir, substantially reducing the pressure gradient between the reservoir and the horizontal well and thereby weakening the driving force for fluid flow. Meanwhile, the overall reservoir temperature declined due to both the latent heat consumption associated with NGH decomposition and the heat removed by produced gas and water. Pressure reduction also induced pore water intrusion from the underburden layer, partially compensating for the energy deficit and sustaining NGH decomposition. Consequently, the primary NGH decomposition front was laterally constrained to a physical scale of approximately 109 m from the production well, with its vertical propagation reaching the upper boundary of the NGH-bearing reservoir. However, as the sensible heat of the formation was rapidly depleted, most regions beyond 109 m of the gas-producing well no longer satisfied the thermodynamic conditions for further NGH decomposition. As a result, NGH decomposition became increasingly localized, primarily occurring near the bottom boundary below the horizontal wellbore.

During Stage C (day 500), Fig. 4(c) illustrates that the NGH decomposition zone was observed to propagate laterally across the entire reservoir (as indicated by the green line at the bottom of the NGH-bearing reservoir). Near the horizontal gas-producing well, NGHs were almost completely decomposed due to favorable thermodynamic conditions. However, as reservoir sensible heat became rapidly depleted, most of the energy for further decomposition must be supplied from the surrounding environment. This process was constrained by the limited heat transfer capacity of the reservoir, resulting in a gradual decline in decomposition efficiency. During this stage, heat input from the underburden layer became increasingly important, with upward intrusion of relatively warm water helping to compensate for heat loss and mitigating the decline in gas production.

By Stage D (day 1000), as indicated in Fig. 4(a) and (b), most of the reservoir no longer satisfied the pressure–temperature conditions required for further NGH decomposition. The pressure drop had propagated throughout the underlying formation, but the limited heat transfer capacity of this layer constrained its contribution to further NGH decomposition. Consequently, as shown in Fig. 4(d), hydrate-derived gas production continued to decline, and the remaining gas accumulated near the top-center of the reservoir due to buoyancy, pressure gradients, and caprock trapping. This gas accumulation briefly enhanced gas production between days 542–652, but as the pressure differential became insufficient to overcome buoyancy forces, the production well was unable to effectively extract gas from this region, resulting in another decline. By the end of the simulation, 16.0% of the NGHs in the reservoir have decomposed, of which 7.1% remained unproduced, yielding a final recovery factor of 14.87%.

3.1.2. Sediment deformation

The exploitation of NGH-bearing reservoirs can lead to the deformation of the geological sediments, primarily due to two mechanisms. (1) Loss of structural support from NGH decomposition: NGH acts as a cementing agent that enhances the mechanical strength of sediments. During exploitation, the decomposition of NGHs reduces this structural support, weakening the reservoir and making it more susceptible to deformation. (2) Reduction in pore water pressure and pore volume compression: Pore water within the sediments supports a portion of the overburden stress. According to Terzaghi's consolidation theory, depressurization and water extraction reduce the pore pressure, increasing the effective stress borne by the sediment skeleton. This results in compaction of the sediment particles and shrinkage of pore volume, particularly when the low-compressibility pore water is lost. These deformation processes can cause seabed subsidence and wellbore instability, necessitating a detailed assessment of the geological risks associated with the NGH production via depressurization.

Fig. 5(a) illustrates the spatiotemporal evolution of sediment subsidence in the base case. Subsidence initiated around the horizontal section of the production well and spread outward, forming a symmetrical distribution along $x = 0$ m. During the initial 50 days of NGH production, the maximum sediment subsidence remained below 1 m, although noticeable deformation occurred near the production well. With ongoing production, settlement accumulated progressively, and, by day 1000, seabed subsidence reached 4.6–4.8 m, posing a significant risk to subsea infrastructure such as wellheads, pipelines, and foundation systems. This highlights the urgent need for effective mitigation strategies during NGH exploitation. Differential subsidence insulted in deformation of different sediment layers. The subsidence difference in vertical displacement between the seabed and the upper boundary of the reservoir reflects the overburden deformation. Similarly, the displacement difference between the reservoir's upper and lower boundaries indicates the internal reservoir deformation, while the displacement of the reservoir's lower boundary represents underburden deformation.

Fig. 5(b) further visualizes the vertical displacement of the seabed and of the upper and lower boundaries of the NGH-bearing reservoir over time, showing that the greater difference between

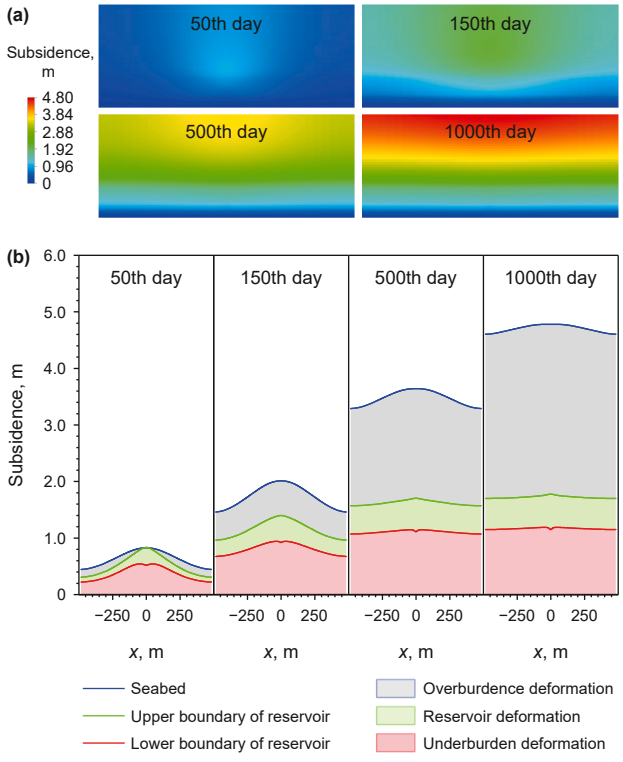


Fig. 5. (a) Spatiotemporal evolution of sediment subsidence and **(b)** sediment deformation at different stages in the base case.

two boundary curves caused the larger compressive deformation of the corresponding layer. As shown in Fig. 4(b), by day 50, pore pressure drop had propagated throughout the reservoir, triggering overall compression. Near the production wells, NGH decomposition reduced sediment strength, leading to pronounced settlement within the decomposition zone. Significant deformation was also observed in the underlying formation beneath the wells, primarily due to the compaction from pore water extraction. Throughout the simulation, the reservoir's lower boundary at $x = 0$ m experienced pronounced subsidence caused by the upward vertical pressure gradient, partially counteracting the downward effective stress. With time, subsidence of the seabed and reservoir boundaries continued to increase, but deformation gradually stabilized as pore pressure equilibrated within the reservoir. Consequently, compressive deformation increased progressively in all three layers. By day 1000, the maximum vertical deformations of the overburden layer, NGH-bearing reservoir, and underburden layer are 3.03 m, 0.63 m, and 1.19 m, corresponding to 1.08%, 1.04%, and 2.37% of their initial thicknesses, respectively. These results indicate that the underburden layer exhibited the highest relative deformation. Although its mechanical strength was assumed equal to that of the overburden layer, its higher permeability facilitated pore water loss, and combined with its lower mechanical strength relative to the NGH-bearing reservoir, made it particularly prone to compaction and deformation.

As illustrated in Fig. 5(b), the non-uniform subsidence of the seabed over time led to the gradual development of reservoir slopes. To quantitatively characterize this process, the seabed slope angles along the *x*-direction were extracted and plotted in Fig. 6(a). Because the subsidence was symmetrically distributed with respect to $x = 0$ m, the maximum vertical displacement occurred at the center, where the slope angle remained zero. Away from the centerline, differential subsidence generated local slopes that evolved dynamically as pore pressure was redistributed. The location of the maximum seabed slope shifted outward from $x = 0$ m (blue arrows in Fig. 6(a)), reflecting the outward diffusion of pore pressure gradients. Fig. 6(b) shows the temporal evolution of the maximum seabed slope angle. Initially, the slope angle increased rapidly during the early production stage, rising from 0° to a peak of 0.097° by day 140, corresponding to the stage of sharp pore pressure decline and pronounced reservoir compaction near the gas production well. With progressive pressure equilibration, the slope angle gradually decreased to 0.032° by day 1000, reflecting a reduction in differential subsidence and a tendency toward mechanical and hydraulic equilibrium. This transient rise–fall pattern demonstrates that seabed slope evolution is closely governed by pore pressure redistribution under depressurization. Importantly, the results indicate that the risk of seafloor instability or submarine landslides does not monotonically intensify with production time. Instead, the hazard is most critical during the early-to-intermediate production stage, when pore pressure gradients and differential settlements are strongest. Over the long term, as the reservoir reaches a near-uniform pore pressure state, the likelihood of large-scale slope failure is substantially reduced. Nevertheless, even small slope angles may become critical under unfavorable geological or environmental conditions (such as weak sediment layers, seismic activity, or ocean currents), emphasizing the importance of site-specific geological risks assessment and proactive risk mitigation during NGH exploitation.

3.1.3. Wellbore integrity

Sediment subsidence and strain induced by the depressurization process, extending from the reservoir interval down to the seabed, represent critical geomechanical hazards that may significantly threaten the stability and operational longevity of subsea infrastructure. Such subsurface deformations can lead to misalignment, mechanical failure, or even collapse of critical components, thereby compromising the overall integrity of the gas production system. Of particular concern is the potential risk posed to the wellbore integrity due to depressurization-induced NGH production. As reservoir pressure declines during production, NGHs destabilize and decompose into gas and water. This decomposition process is often accompanied by significant volume expansion and alterations of the in-situ stress regime, which can trigger localized or widespread sediment movement. The resulting vertical subsidence and induced strains, particularly around the wellbore, can adversely affect well integrity.

In the base case, the vertical segment of the production well was situated between depths of $z = 70$ m and $z = 390$ m along the $x = 0$ m profile. This interval is identified as the most geomechanically sensitive portion of the well and is therefore of primary concern when assessing mechanical stability under

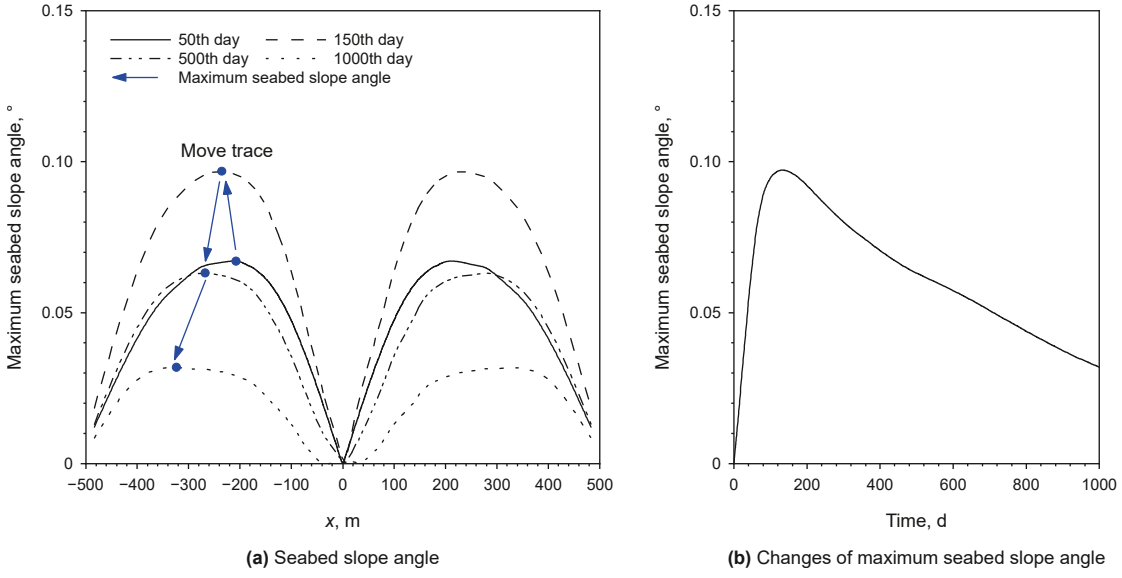


Fig. 6. **(a)** Distribution of the seabed slope angles and **(b)** temporal evolution of the maximum slope angle.

depressurization. To evaluate the wellbore's mechanical stability, we monitored the vertical distributions of sediment subsidence and axial strain along this segment. These parameters are shown in Fig. 7, which provides a detailed profile of how the seafloor and subsurface strata respond mechanically to the pressure drawdown. In Fig. 7, the vertical axis (z) corresponds to depth, while the plotted values denote the magnitude and direction of strain in the surrounding sediments. It is important to note that in this context, positive strain values indicate compressive deformation, whereas negative strain values signify tensile deformation. Such tensile strains are particularly critical, as they may approach or exceed the tensile strength of the formation or cement sheath, increasing the likelihood of micro-fracturing or wellbore collapse.

Fig. 7 reveals that strains in the reservoir and the underburden layer remained consistently positive throughout the depressurization-induced NGH production process, indicating that these formations were primarily subject to compressive deformation. This compressive behavior is primarily driven by the reduction in pore pressure as NGHs dissociate and release gas and water, which increases effective stress and causes the sediment matrix to compact. In contrast, the overburden layer exhibited localized negative strains, representing tensile deformation, during the first 50 days of production. This tensile response is likely due to the rapid initial drop in reservoir pressure, which resulted in a transient stress redistribution. Being less directly affected by the immediate decompression of the reservoir, the overburden layer initially experienced a stretching effect, especially near its interface with the NGH-bearing reservoir, before gradually stabilizing as the system approaches a new equilibrium state. Furthermore, as demonstrated in Fig. 4, the zones within the reservoir that exhibited the most pronounced strain values closely coincide with regions of NGH decomposition. These are the areas where the decomposition process was most active, leading to significant changes in the sediment's physical properties, including a marked reduction in mechanical strength. NGH decomposition not only releases gas and increases pore fluid volume but also alters the sediment fabric, reducing cohesion and increasing pore pressure in localized zones, all of which contribute to enhanced strain localization. The presence of such high-strain zones indicates potential vulnerability in the reservoir structure, where the risk of shear failure, compaction-induced fracturing, or wellbore deviation may be elevated. Additionally, the strain profiles in Fig. 7 display sharp gradients at both the upper and lower boundaries of the reservoir. These abrupt changes are attributed to the mechanical contrast between the relatively strong NGH-bearing reservoir and the comparatively weaker overburden and underburden layers. The overburden, typically composed of less consolidated or more porous sediments, has lower shear strength and stiffness, making it more prone to tensile deformation or differential movement. Similarly, although generally stronger than the overburden, the underburden layer can still experience localized failure or compaction under increased effective stress, especially near the reservoir boundary where stress concentrations are high. These mechanical contrasts amplify the strain gradients across the interfaces, creating zones of concentrated deformation that may influence the overall stability of the wellbore. The observed subsidence, which represents the cumulative vertical displacement from the deepest to the shallowest layers, is a direct consequence of the integrated vertical strain across the stratigraphic column. As illustrated in Fig. 7, subsidence increased gradually from the bottom upward in the early stages of production and subsequently decreases. This non-monotonic behavior reflects the combined effects of reservoir compaction and overburden tension, and illustrates the dynamic adjustment of the geomechanical system as the pressure drop propagates. Such behavior underscores the dynamic nature of sediment response during NGH production and highlights the importance of monitoring sediment deformation over time. Given these observations, horizontal well depressurization strategies must pay special attention to deformation behavior at the reservoir's upper boundary, where the transition from the reservoir to the overburden occurs. This region is particularly critical, as it not only experiences significant strain gradients but also represents the zone where the wellbore transitions from its horizontal to vertical orientation, often the most structurally sensitive segment. Deformation in this area, if not properly managed, could lead to misalignment between well casing and the surrounding formation, potentially resulting in well casing damage, loss of zonal isolation, or even wellbore dislocation. Such mechanical dislocation can compromise the sealing integrity of the well, increase the risk of gas or fluid migration along the annulus, and ultimately jeopardize the safety and efficiency of the production operation.

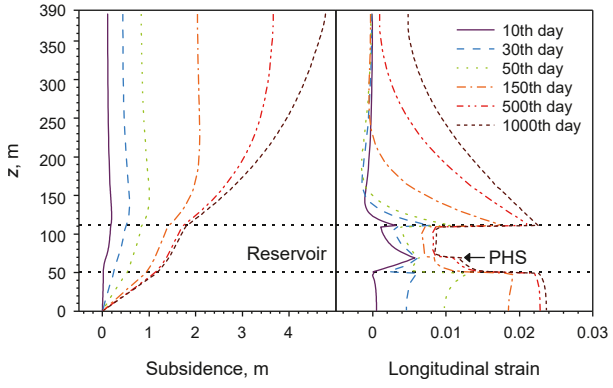


Fig. 7. Vertical profiles of subsidence and strain at $x = 0$ m in the base case.

Therefore, to ensure the long-term integrity and operational reliability of the production well, it is essential to integrate detailed geomechanical modeling with real-time monitoring of subsurface deformation. Strategies such as optimized well placement, enhanced casing and cementing designs, controlled depressurization rates, and the use of flexible or expandable wellbore architectures should be considered to mitigate the adverse effects of strain localization and differential movement. Moreover, proactive measures to manage stress arching, reinforce critical interfaces, and accommodate potential wellbore-seafloor interaction are crucial in minimizing the risk of structural failure. In summary, the findings illustrated in Figs. 4 and 7 collectively emphasize the complex interplay between NGH decomposition, sediment deformation, and wellbore integrity, highlighting the need for a geomechanically informed approach to the design and operation of hydrate production systems.

3.2. Effect of bottom-hole pressure (BHP)

This section conducted a systematic investigation into the influence of BHP on both gas production efficiency and geomechanical safety during the depressurization process of NGH-bearing reservoirs via horizontal-well. A comprehensive analysis was carried out across six discrete BHP levels, specially ranging from 3 MPa to 8 MPa, which were denoted as BHP3–BHP8. To ensure that the observed effects can be accurately attributed to pressure variations and to eliminate the confounding influence of well-geometry factors, the well geometry was meticulously kept constant throughout the study. In this setup, the horizontal section of the well was positioned 20 m above the reservoir base, at a

depth of $z = 70$ m. This fixed well-geometry configuration provides a stable and consistent framework for isolating and analyzing the sole impact of BHP on the production processes within the NGH-bearing reservoir.

3.2.1. Effect on gas and water production

The variations in cumulative gas and water production over time under different BHPs are illustrated in Fig. 8. A distinct relationship between BHP and production is demonstrated. Specifically, lower BHPs were consistently associated with higher cumulative gas and water production at any given time. By the 1000th day of the production process, the BHP3 case, which represented the lowest BHP level among the six studied, achieved the highest gas production of 1.22×10^6 m^3, in sharp contrast, the BHP8 case, corresponding to the highest BHP level, yielded the lowest gas production of only 0.16×10^6 m^3. This large difference in gas production clearly highlights the strong influence of BHP on the gas-releasing process within the NGH-bearing reservoir.

Fig. 9 further presents the gas recovery ratio and gas–water ratio on the 1000th day. The gas recovery ratio is a key metric that reflects the proportion of the total recoverable resources that have been successfully extracted from the reservoir. The gas-water ratio, on the other hand, provides insights into the relative amounts of gas and water produced, which has important implications for the economic viability of the NGH production process. The results shown in Fig. 9 indicate that lower BHPs result in higher gas recovery ratios and gas-water ratios. A higher gas recovery ratio means that a larger proportion of the gas stored in the NGHs has been successfully extracted, while a higher gas-water ratio implies that a greater amount of gas is being produced relative to water. These two factors combined offer improved economic performance as a higher gas recovery ratio maximizes the extraction of the valuable gas resource, and a higher gas-water ratio reduces the handling and disposal costs associated with water production. This observed phenomenon can be attributed to the fact that lower BHP accelerates the decomposition of NGHs, and that gas production is more sensitive to pressure variations than water production. As the BHP decreases, gas can be more easily released from the gas hydrate structure, resulting in a faster

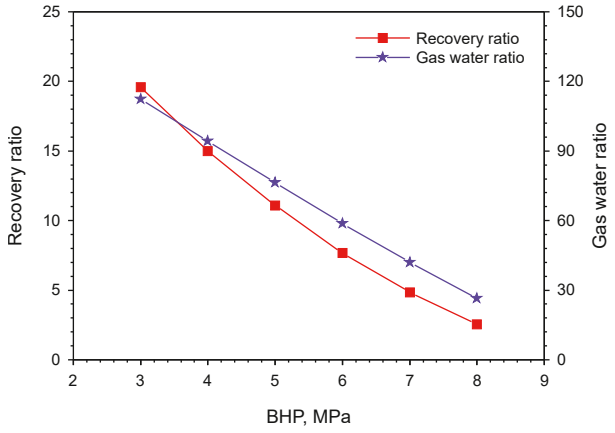
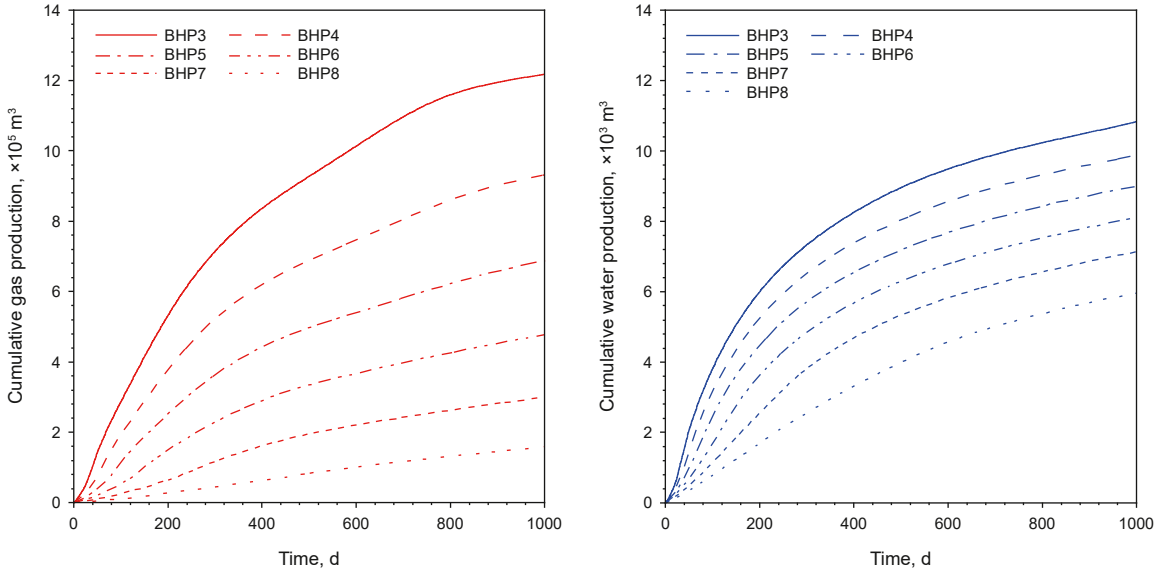


Fig. 9. Gas recovery ratio and gas–water ratio on the 1000th day under different BHPs.

increase in gas production than water production. This differential sensitivity of gas and water production rates to pressure changes is the fundamental reason why lower BHPs lead to higher cumulative gas and water production, as well as improved gas recovery and gas-water ratios.

Fig. 10 shows the spatial distribution of NGH saturation in the reservoir on the 1000th day for different BHPs. By examining the spatial patterns of NGH saturation, valuable insights can be acquired into the extent and distribution of NGH decomposition within the reservoir. It is evident that lower BHPs lead to more extensive NGH decomposition. Specifically, as the BHP was increased gradually from 3 MPa to 8 MPa, the lateral extent of the completely dissociated NGH zone was 224.33, 174.86, 140.21, 109.363, 85.53, and 58.89 m, separately. When the BHP is relatively low, the equilibrium state of the NGHs in the reservoir is significantly disrupted. According to the principles of thermodynamics, NGHs are stable within a specific range of pressure and temperature. A decrease in BHP pushes the system out of this stability range, initiating the decomposition process of NGHs into gas and water. As the BHP drops further, the driving force for NGH decomposition becomes stronger. This results in a more



(a) Cumulative gas production **(b)** Cumulative water production

Fig. 8. Cumulative gas and water production over time under different BHPs.

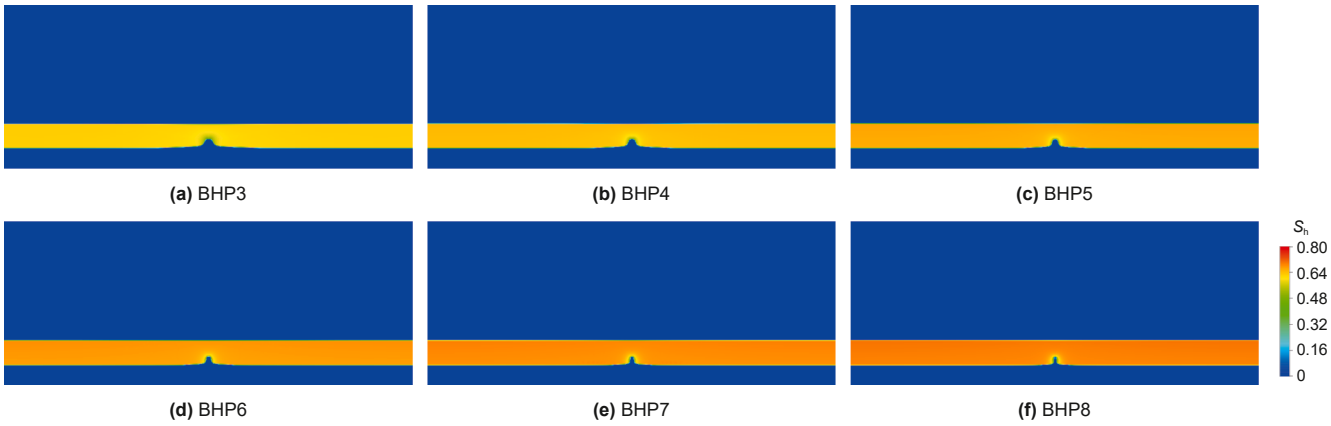


Fig. 10. Distributions of NGH saturation in the reservoir on the 1000th day under different BHPs.

widespread breakdown of NGHs throughout the reservoir. For example, in the case of BHP3, which represent the lowest BHP levels, the areas with lower NGH saturation (indicating more NGH decomposition) are more extensive compared to the case of BHP with the highest BHP levels. However, even under low BHP conditions, NGH decomposition is largely confined to the region directly beneath the horizontal section of the producer well. This spatial confinement of NGH decomposition is a critical factor that influences the overall gas recovery efficiency. The producer well serves as the primary pathway for the extraction of gas and water from the reservoir. The pressure drawdown created by the production process is most significant in the vicinity of the wellbore. As a result, the effect of the low BHP is most pronounced in the area directly beneath the horizontal section of the well. The high-permeability zone around the wellbore allows for easier fluid flow, facilitating the decomposition of NGHs in this region. But as we move away from the wellbore, the pressure drawdown gradually decreases, and the influence of the low BHP becomes less significant.

3.2.2. *Effect on geomechanical stability*

Fig. 11 illustrates the sediment subsidence occurring on the 1000th day under different BHP conditions. This visual representation is crucial for understanding how varying BHP levels impact the geological risks of the sediment layers during NGH production. As the BHP increased from 3 MPa to 8 MPa, the sediment subsidence consistently and significantly decreased across all layers, showing a clear inverse relationship. At relatively low BHP, the pore pressure in the reservoir decreases significantly, resulting in a larger pressure drawdown. This increases the effective stress acting on the sediment particles, causing them to be more compacted. Meanwhile, low BHP also promotes extensive NGH decomposition. The decomposition releases gas and water, and the extracted gas and water further reduces the pore pressure. Together, the increase in effective stress and the reduction in pore pressure leads to significant sediment compaction and subsidence. By contrast, at higher BHP, such as at BHP8, the reservoir pore pressure decreases only slightly, helping maintain mechanical stability within the reservoir. Because the overall pressure environment is less disturbed, the effective stress on sediment particles does not increase significantly. In addition, higher BHP suppresses NGH decomposition. Since NGH decomposition is the primary factor leading to the release of gas and water and the associated changes in sediment properties, a lower degree of decomposition keeps pore water content relatively stable, thereby limiting both effective stress increase and sediment subsidence.

Fig. 12 presents the maximum seabed subsidence and slope angle over a 1000-day production period under various BHP scenarios. Both parameters decreased notably as BHP increases. This

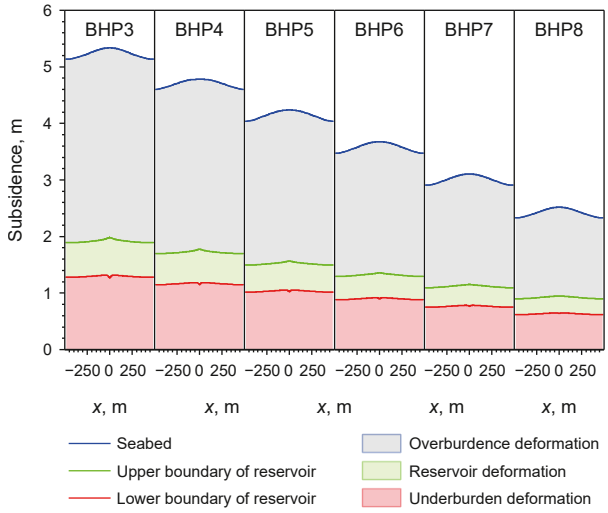


Fig. 11. Sediment subsidence on the 1000th day under different BHP levels.

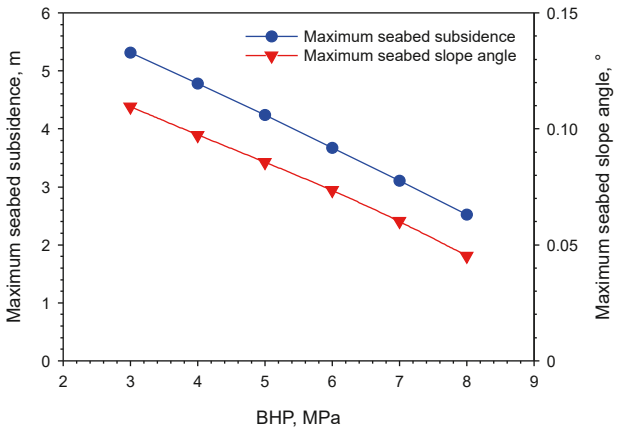


Fig. 12. Maximum seabed subsidence and slope angle under different BHP levels.

decreasing trend is a clear indication of the positive impact of higher BHP on seabed stability. When BHP increased from 3 MPa to 8 MPa, the maximum seabed subsidence declined from 5.31 m to 2.52 m, representing a significant reduction. Similarly, the maximum slope angle reduced from 0.11° to 0.045°, which was a reduction of over 50%. These results indicate that a higher BHP effectively alleviates effective stress buildup and mitigates pressure heterogeneity within the sediment, thereby reducing the risk of excessive seabed deformation and slope instability. At low BHP, a large pressure drawdown between the wellbore and the surrounding sediments significantly increases effective stress, leading to differential settlement and the formation of slopes. In contrast, higher BHP maintains a more stable reservoir pressure, limiting stress increases and reducing sediment compression. Furthermore, pressure heterogeneity under low BHP conditions can cause uneven stress distribution, resulting in differential settlement and slope formation. Higher BHP helps to minimize this pressure heterogeneity, ensuring a more uniform stress field and thereby reducing slope instability. The significant reductions in maximum seabed subsidence and slope angle with increasing BHP highlight the importance of carefully managing the BHP during NGH production. Maintaining an appropriate BHP not only ensures the gas production efficiency but also enhances long-term seabed stability and safe offshore operations. This has far-reaching implications for the sustainable development of offshore NGH resources.

3.2.3. Effect on wellbore integrity

Fig. 13 shows the distributions of sediment subsidence and strain along the z-direction at $x = 0$ m in the sediment on the 1000th day under different BHP levels. The results show that as BHP decreased, both sediment subsidence and the associated vertical strain intensified at all depths along the production well, indicating that lower BHPs amplified the deformation response of the surrounding strata. Specifically, when the BHP decreased from 8 MPa to 3 MPa, the vertical strain at the seabed increased from 0.002 m to 0.005 m, reflecting a substantial weakening of the sediment's resistance to deformation. These results suggested lower BHP levels significantly elevate the risk of wellbore deformation and structural instability. The underlying mechanism is associated with enhanced NGH decomposition, higher gas and water production, and redistribution of effective stress caused by low BHP levels. The resulting increase in subsidence and strain along the entire vertical profile poses significant risks to the wellbore integrity. Although the wellbore is typically cased and cemented to maintain stability, excessive vertical strain observed at low BHP may lead to casing deformation, cement sheath failure, or even wellbore collapse. These structural issues not only impact operational efficiency but also heighten the potential for catastrophic failures, such as uncontrolled fluid release.

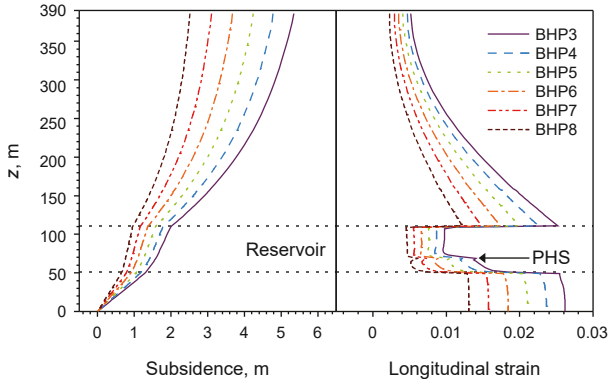


Fig. 13. Vertical profiles of sediment subsidence and vertical strain at $x = 0$ m on the 1000th day under different BHP levels.

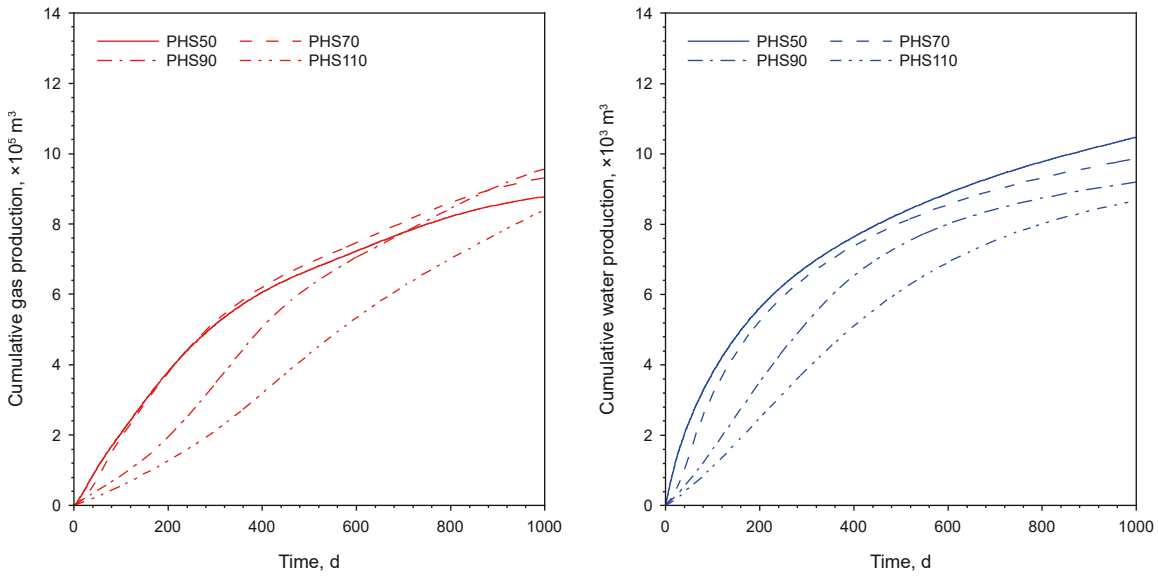
In summary, the findings from Figs. 8–13 collectively underscore a critical trade-off: while lower BHP can enhance the gas production efficiency, it also increases the risk of wellbore deformation and structural degradation. Careful BHP management is therefore essential for NGH exploitation. Maintaining a minimum BHP threshold, implementing strain-monitoring systems, and reinforcing wellbore casings in high-strain zones are potential strategies to balance production optimization with long-term well stability.

3.3. Effect of horizontal well location

This section systematically investigated how the placement elevation of PHS influences gas production efficiency and geological risks during horizontal-well depressurization of NGH-bearing reservoirs. While maintaining a constant BHP of 4 MPa to isolate the effect of well placement, four distinct PHS elevations were evaluated, spanning from the reservoir base (PHS50 at $z = 50$ m) to near the upper boundary (PHS110 at $z = 110$ m).

3.3.1. Effect on gas and water production

Fig. 14 shows the cumulative gas and water production over time at different PHS elevations. As the PHS depth varied from 50 m (reservoir bottom) to 110 m (reservoir top) along the z-direction, the cumulative gas production exhibited a non-monotonic trend across the evaluation period, reflecting the complex interplay between well placement, NGH decomposition, and gas production behavior. During the first 500 days, cumulative gas production showed distinct grouping patterns. PHS50 (bottom) and PHS70 (lower-middle) displayed similar production trajectories with the fastest gas production rates, followed by PHS90 (upper-middle), while PHS110 (top) consistently lagged behind. After 500 days, the gas production dynamics shifted significantly. PHS50 gradually fell below PHS70, and PHS90 experienced a marked acceleration, eventually surpassing both PHS50 and PHS70 to become the most productive scenario by the end of the simulation. PHS110 remained the lowest-producing case throughout. By day 1000, PHS90 achieved the highest cumulative gas production (9.57×10^5 m^3), while PHS110 recorded the lowest (8.41×10^5 m^3), corresponding to a 13.8% variation. These phenomena can be attributed to the NGH decomposition mechanism induced by the intrusion of warm water from the underlying layer into the NGH reservoir, as discussed in Section 3.1.1. PHS50 and PHS70, located close to the underburden layer, allow warm water to penetrate the hydrate reservoir with minimal resistance, promoting rapid NGH decomposition and sustaining high gas production during the early stages. In contrast, PHS90, being farther from the underburden layer, experiences limited warm water intrusion initially, leading to slower gas production. However, as NGH decomposition around the PHS90 wellbore progresses, reservoir permeability increases, enabling accelerated warm water intrusion in the later stages. This process markedly enhances NGH decomposition and ultimately allows PHS90 to surpass the other cases in gas production efficiency. By comparison, PHS110, situated near the reservoir's upper boundary, is minimally influenced by warm water intrusion and therefore maintains consistently low gas production throughout the evaluation period. In terms of water production, lower PHS positions yield higher cumulative output: PHS50 produces 10.4×10^3 m^3, compared with 8.67×10^3 m^3 at PHS110, representing a 20% increase. This difference arises because lower positions are more prone to intrusion of warm water from the underburden layer, while gravity further promotes water accumulation at deeper levels. These results



(a) Cumulative gas production **(b)** Cumulative water production

Fig. 14. Cumulative gas and water production over time under different PHS locations.

highlight that a reasonable PHS placement requires balancing early- and late-stage gas production.

The economic implications of these trends are further elucidated in Fig. 15, which displays the gas recovery ratio and gas–water ratio on the 1000th day for various PHS locations. The PHS90 case achieved the optimal configuration, achieving the highest gas recovery ratio and gas–water ratio. This indicates that positioning the well slightly above the mid-depth of the reservoir maximizes gas extraction while minimizing water co-production, thereby enhancing overall economic performance. In practical operations, however, the gas production efficiency and gas-water ratio must be considered comprehensively from both short-term and long-term perspectives.

To further explain the gas production behavior in Figs. 14(a) and 16 illustrates the spatial distribution of NGH saturation in the reservoir on the 1000th day for different PHS placements. NGH decomposition was concentrated around the production well and at the region between the NGH-bearing reservoir and the underburden layer, where wellbore depressurization and

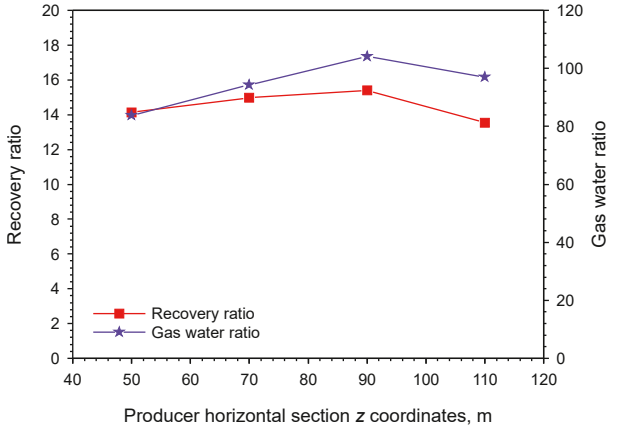


Fig. 15. Gas recovery ratio and gas–water ratio on the 1000th day for different PHS locations.

warm water intrusion from the underburden layer create favorable NGH decomposition conditions. However, distinct spatial patterns emerged depending on well placement. In PHS50, NGH decomposition was primarily concentrated at the interface between the NGH-bearing reservoir and the underburden layer. This spatial pattern arises because the low PHS placement facilitates direct contact with the underburden layer, enabling warm water intrusion to dominate the decomposition process. However, the low PHS elevation limits its influence on the upper reservoir, and the decomposition front fails to propagate extensively into the central reservoir. This spatial restriction leads to a gradual decline in NGH decomposition and gas production efficiency during later stages. In PHS70, the combined effects of depressurization and warm water intrusion led to rapid NGH decomposition near the wellbore and adjacent underburden layer. The moderate well depth allowed warm water from the underburden layer to enter the NGH-bearing reservoir, promoting NGH decomposition front to expand more widely than in PHS50. This sustains gas production efficiency over a longer period. In PHS90, with wells located in the upper middle, early NGH decomposition was primarily driven by depressurization near the wellbore. As the decomposition front advanced downward, it eventually connected with the underburden layer, allowing warm water to intrude and provide additional heat. This sequential mechanism—initial depressurization-driven decomposition, followed by thermally enhanced decomposition—creates a persistent, intensified decomposition zone beneath the wellbore. The sequential activation of depressurization and thermal drivers ensures a continuous NGH decomposition, achieving long-term gas production efficiency exceeding that of PHS50 and PHS70. In contrast, PHS110 exhibited the weakest NGH decomposition efficiency. The high elevation and large vertical separation from the underburden prevent the NGH decomposition front from reaching underburden layer within the 1000-day period, limiting warm water intrusion. Consequently, NGH decomposition was driven almost entirely by depressurization and remains confined near the wellbore, resulting in the lowest cumulative gas production. Fig. 16 clearly explains the non-monotonic cumulative gas production trend with PHS elevation shown in Fig. 14(a).

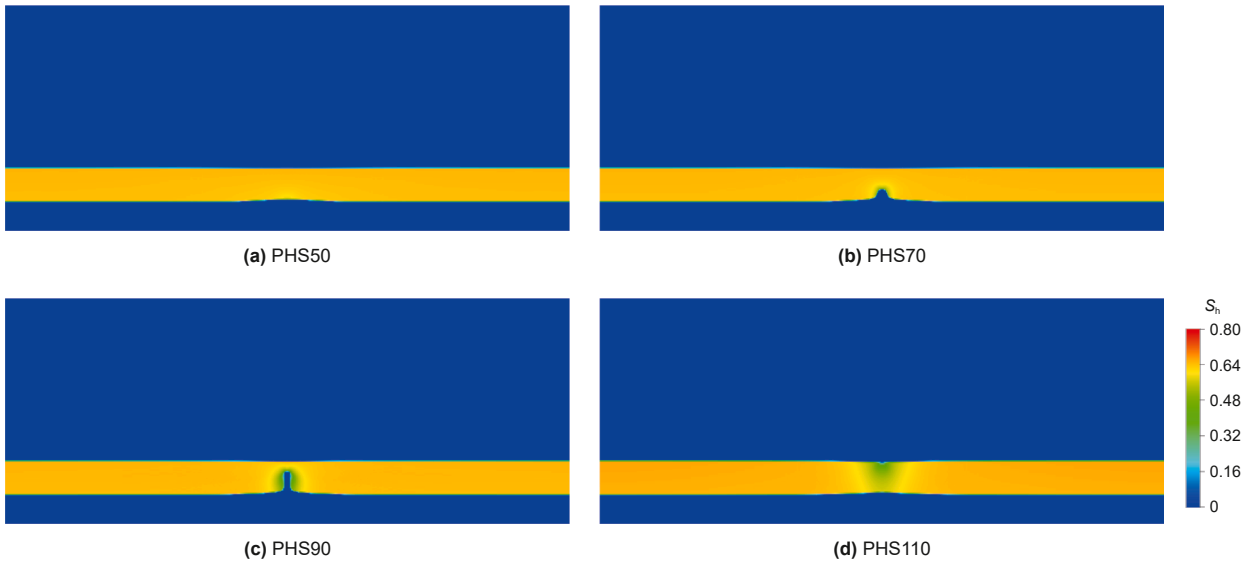


Fig. 16. NGH saturation distribution on the 1000th day for different PHS placements.

In summary, PHS placement is crucial for both short-term production efficiency and long-term recovery in NGH-bearing reservoirs. The spatial positioning of PHS directly impacts the interplay between wellbore depressurization, NGH decomposition kinetics, and warm water intrusion from the underburden layer. These factors collectively determine the sustainability and intensity of gas production. Optimizing PHS placement is therefore essential for achieving efficient and sustainable NGH decomposition. A balanced strategy—such as combining PHS70 and PHS90 in a dual-layer configuration—may offer an effective solution. This approach not only improves initial gas production but also enhances long-term stability and efficiency in gas extraction.

3.3.2. *Effect on geomechanical stability*

The influence of PHS placement on geological risks was evaluated through its impact on sediment stability, seabed deformation, and slope integrity. Fig. 17 shows the sediment subsidence across four PHS elevations on the 1000th day. As the PHS position increased, the subsidence of the underburden layer and NGH-bearing reservoir decreased slightly, indicating that the vertical position of the PHS has minimal impact on the subsidence of these two layers. In this section, gas production pressure remained consistent, and the NGH decomposition zone had spread throughout the reservoir. The subsidence of the underburden layer is primarily determined by cumulative water production. As shown in Fig. 14(b), an increase in PHS position lead to a slight decrease in cumulative water production, which in turn reduced underburden subsidence. Additionally, the subsidence of the NGH-bearing reservoir is influenced by NGH decomposition. Fig. 16 shows that as the PHS position increased, the decomposition zone became more confined to the vicinity of the gas well. This results in greater sediment subsidence near the well compared to areas further away. Furthermore, the increase in effective stress due to water production in the overburden and pressure reduction also contributes to seabed subsidence above the horizontal well. Due to similar cumulative gas and water production, seabed subsidence differed little between PHS50, PHS70, and PHS90, but the seabed slope angle increased slightly. For PHS110, the restricted NGH decomposition zone leads to enhanced differential subsidence of

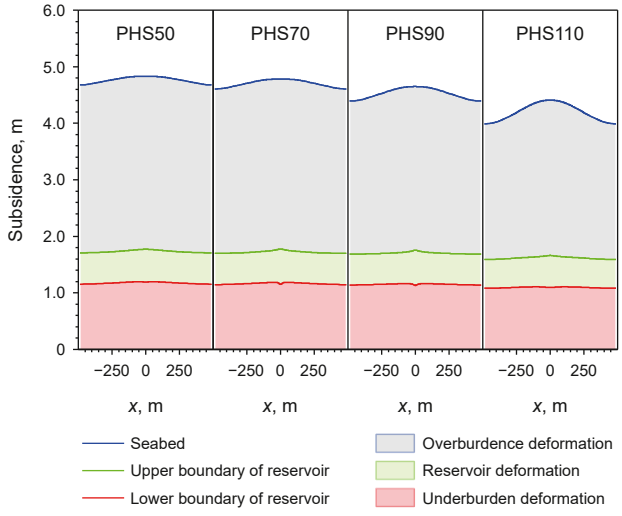


Fig. 17. Sediment subsidence on the 1000th day for different PHS placements.

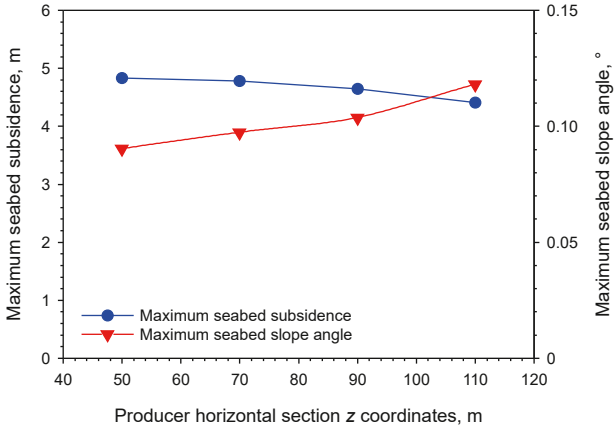


Fig. 18. Maximum seabed subsidence and slope angle under different PHS locations.

the overburden, resulting in a larger seabed slope angle. In general, the effect of PHS placement on sediment subsidence is smaller compared to that caused by changes in BHP.

Fig. 18 illustrates the relationship between PHS placement and two critical seabed stability metrics: maximum seabed subsidence and maximum slope angle. As the PHS was moved from the reservoir bottom (PHS50) to the top (PHS110), the maximum seabed subsidence decreased from 4.82 m to 4.41 m, representing a 9.3% reduction. In contrast, the maximum slope angle increased from 0.09° to 0.118°, a 31% rise. These opposing trends indicate that seabed deformation becomes more heterogeneous with increasing PHS position. As shown in Fig. 7, seabed subsidence was strongly associated with NGH decomposition. Figs. 14 and 17 further demonstrate that higher PHS placements resulted in lower water production, which reduces the effective stress buildup on sediment particles and alleviates reservoir compaction. By contrast, slope angle is more sensitive to heterogeneity in reservoir caused by gas and water production and NGH decomposition. These uneven stresses typically emerge during the early stage of pressure drawdown, leading to localized compaction and slope formation. At lower PHS locations, production well is more likely to intersect the permeable underburden layer, allowing wellbore pressure drop to penetrate through the underburden layer and enhance hydraulic communication between the underburden and NGH-bearing reservoir. This promotes more uniform NGH decomposition throughout the reservoir. At higher PHS placements, however, production well remains isolated from the high-permeability underburden layer during early production, localizing NGH decomposition around the wellbore. This leads to greater vertical subsidence near the well and a steeper seabed slope angle.

3.3.3. Effect on wellbore integrity

To further assess the impact of PHS location on wellbore stability, Fig. 19 presents the vertical distribution of sediment settlement and the corresponding strain along the z-direction at the horizontal midpoint ($x = 0$ m) of the 1000th day. Settlement at all PHS locations was depth-dependent, increasing from the bottom upward, with maximum displacement occurring at the seafloor. While settlement at a given depth increased slightly with higher PHS placement, the overall effect on reservoir settlement was minimal. The strain profiles exhibited abrupt changes at the upper and lower boundaries of the hydrate reservoir, reflecting localized deformation in these zones. Importantly, the vertical strain patterns remained largely insensitive to PHS elevation, indicating that wellbore structural integrity was governed mainly by the intrinsic mechanical properties of the sediment and local effects of NGH decomposition (e.g., pore pressure reduction, gas and water release), rather than the vertical position of the production well. Thus, PHS placement can be optimized primarily for gas production efficiency without imposing additional risks to wellbore stability. Nevertheless, operators should closely monitor seabed subsidence and slope evolution, as these factors may compromise the stability of surface infrastructure (e.g., pipelines, platforms) anchored to the seabed.

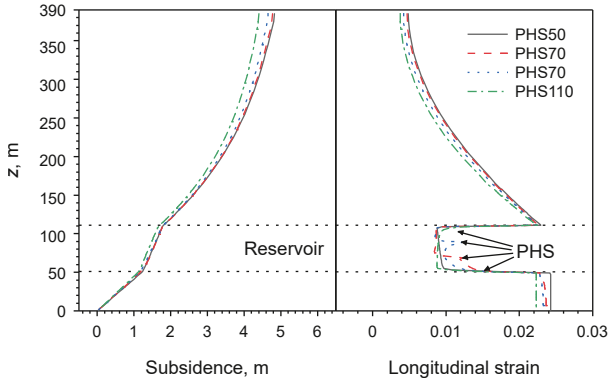


Fig. 19. Vertical distribution of sediment subsidence and strain at $x = 0$ m on the 1000th day under different PHS locations.

3.4. Limitations and future work

While the proposed THMC framework provides critical insights into the geomechanical responses induced by depressurization, it is essential to acknowledge the limitations associated with its coupling strength. Recently, advanced fully coupled THMC models have been developed (Zhang et al., 2025), which strictly incorporate the dynamic feedback of mechanical deformation on porosity and permeability. In contrast, the model utilized in this study adopts a weakly coupled approach, wherein fluid flow and hydrate dissociation drive effective stress alterations, but the resulting volumetric strain does not dynamically update the governing equations for pore-scale fluid transport. This one-way coupling strategy was specifically selected to address the extensive computational demands of the present study. The distinct advantage of the present model lies in its superior computational efficiency and robustness while maintaining reasonable accuracy. This renders it highly applicable for field-scale scenarios requiring long-term production forecasts and the evaluation of large-scale geohazards, such as extensive seabed subsidence and large-scale plastic yielding around horizontal wells (Chin et al. 2011; Rutqvist et al., 2012; Saffou et al., 2023).

Nevertheless, the omission of deformation-porosity feedback inevitably introduces certain computational deviations. Specifically, in the near-wellbore region, the substantial increase in effective stress during depressurization induces severe sediment compaction. By neglecting this compaction-induced permeability reduction, the present weakly coupled model may slightly overestimate fluid mobility and long-term gas recovery rates. Future research will focus on the development and integration of advanced algorithms capable of achieving higher coupling strength, while preserving the computational efficiency requisite for comprehensive field-scale parametric studies.

4. Conclusions

In this study, a thermal–hydrological–mechanical–chemical (THMC) model coupled with the Drucker–Prager yield criterion was developed to evaluate the geomechanical responses induced by natural gas hydrate (NGH) exploitation. The impacts of bottom-hole pressure (BHP) and the vertical positioning of the PHS on sediment stability and geological risk were systematically analyzed. The following conclusions are drawn.

1. Horizontal-well depressurization significantly accelerates the decomposition of natural gas hydrates, with gas production evolving through four distinct stages: rapid rise, sharp decline, gradual decline, and low production. In the base case, cumulative gas recovery reaches 9.31×10^5 m^3 over 1000 days, corresponding to a recovery factor of 14.87%. Lower bottom-hole pressure and mid-depth placements of producer horizontal section yield more sustained and higher production rates.
2. Sediment subsidence and the formation of seabed slopes are found to be primarily governed by pore pressure reduction and the loss of hydrate-induced structural support. It is demonstrated that lower BHP levels amplify strain localization near the wellbore, significantly increasing risks to wellbore stability

and overlying seabed infrastructure. While the elevation of producer horizontal section has minimal influence on reservoir strain, higher placements of producer horizontal section enhance subsidence heterogeneity at the seafloor, resulting in intensified differential subsidence and slope instability.

3. An optimal balance between production efficiency and geomechanical safety is achieved by maintaining BHP above a critical threshold of 4–5 MPa to mitigate excessive deformation. Additionally, positioning the PHS near the reservoir mid-depth ($z = 70$–90 m) is found to be the most effective strategy to utilize the thermal energy of intruded underburden water while preserving formation integrity for long-term gas production.

The results of this study underscore the necessity of integrating real-time deformation monitoring with adaptive well designs to mitigate long-term risks under complex geological constraints. These findings provide critical technical support for the development of safe exploitation protocols, facilitating the transition of NGH resources toward commercial viability.

CRediT authorship contribution statement

Shu-Yang Liu: Writing – review & editing, Funding acquisition, Conceptualization. **Qi-Zhi Tan:** Writing – original draft, Formal analysis. **Chen Fan:** Methodology. **Zhi-Qiang Wang:** Visualization. **Zhi-Yuan Wang:** Investigation. **Jing-Sheng Lu:** Data curation. **Shu-Xia Li:** Software. **Bin Wang:** Writing – review & editing.

Declaration of competing interest

The authors declare that they have no known competing financial interests or personal relationships that could have appeared to influence the work reported in this paper.

Acknowledgements

This paper has been financially supported by the National Natural Science Foundation of China (No. 52574072 and No. 42376215), Key Laboratory of Gas Hydrate, Ministry of Natural Resources (No. KLGH-2023-07) and Guangdong Provincial Key Laboratory of New and Renewable Energy Research and Development (No. E439kf0701), which are gratefully acknowledged.

References

Akaki, T., Kimoto, S., Oka, F., 2016. Chemo-thermo-mechanically coupled seismic analysis of methane hydrate-bearing sediments during a predicted Nankai Trough Earthquake. Int. J. Numer. Anal. Methods GeoMech. 40 (16), 2207–2237. https://doi.org/10.1002/nag.2527.

Chin, L.Y., Silpngarmlert, S., Schoderbek, D.A., 2011. Subsidence prediction by coupled modeling of geomechanics and reservoir simulation for methane hydrate reservoirs. In: Proceedings of 45th U.S. Rock Mechanics/Geomechanics Symposium. ARMA-11-307.

Chong, Z.R., Yang, S.H.B., Babu, P., et al., 2016. Review of natural gas hydrates as an energy resource: prospects and challenges. Appl. Energy 162, 1633–1652. https://doi.org/10.1016/j.apenergy.2014.12.061.

Cui, J., Wang, X., Li, Y., et al., 2024. Influence of gravity on methane hydrate dissociation characteristics by depressurization in marine hydrate reservoirs. Energy 296, 131133. https://doi.org/10.1016/j.energy.2024.131133.

Dong, L., Li, Y., Liao, H., et al., 2020. Strength estimation for hydrate-bearing sediments based on triaxial shearing tests. J. Petrol. Sci. Eng. 184, 106478. https://doi.org/10.1016/j.petrol.2019.106478.

Dong, L., Liao, H., Li, Y., et al., 2022. Analysis of the mechanical properties of the reconstituted hydrate-bearing clayey-silt samples from the South China Sea. J. Mar. Sci. Eng. 10 (6), 831. https://doi.org/10.3390/jmse10060831.

Dong, S., Yang, M., Zhang, L., et al., 2023. Methane hydrate exploitation characteristics and thermodynamic non-equilibrium mechanisms by long depressurization method. Energy 280, 128178. https://doi.org/10.1016/j.energy.2023.128178.

Feng, Y., Chen, L., Suzuki, A., et al., 2019. Numerical analysis of gas production from reservoir-scale methane hydrate by depressurization with a horizontal well: The effect of permeability anisotropy. Mar. Petrol. Geol. 102, 817–828. https://doi.org/10.1016/j.marpetgeo.2019.01.041.

Fu, Q., Pang, W., Chen, M., et al., 2025. Laboratory-scale natural gas hydrate extraction numerical simulation under phase transition effect. Energies 18 (3), 755. https://doi.org/10.3390/en18030755.

Gajanayake, S.M., Gamage, R.P., Li, X.-S., et al., 2023. Natural gas hydrates – insights into a paradigm-shifting energy resource. Energy Rev. 2 (1), 100013. https://doi.org/10.1016/j.enrev.2022.100013.

Gong, G., Yang, M., Liang, Q., et al., 2025. Enhancing real-time gas production from muddy methane hydrate reservoirs: the impact of optimal production pressure. Energy 333, 137401. https://doi.org/10.1016/j.energy.2025.13740.

Hyodo, M., Wu, Y., Nakashima, K., et al., 2017. Influence of fines content on the mechanical behavior of methane hydrate-bearing sediments. J. Geophys. Res. Solid Earth 122 (10), 7511–7524. https://doi.org/10.1002/2017JB014154.

Jin, G., Lei, H., Xu, T., et al., 2018. Simulated geomechanical responses to marine methane hydrate recovery using horizontal wells in the Shenhu area, South China Sea. Mar. Petrol. Geol. 92, 424–436. https://doi.org/10.1016/j.marpetgeo.2017.11.007.

Jin, G., Su, Z., Zhai, H., et al., 2023. Enhancement of gas production from hydrate reservoir using a novel deployment of multilateral horizontal well. Energy 270, 126867. https://doi.org/10.1016/j.energy.2023.126867.

Konno, Y., Fujii, T., Sato, A., et al., 2017. Key findings of the world's first offshore methane hydrate production test off the coast of Japan: Toward future commercial production. Energy & Fuels 31 (3), 2607–2616. https://doi.org/10.1021/acs.energyfuels.6b03143.

Kurihara, M., Sato, A., Funatsu, K., et al., 2010. Analysis of production data for 2007/2008 Mallik gas hydrate production tests in Canada. In: Proceedings of SPE International Oil and Gas Conference and Exhibition in China. https://doi.org/10.2118/132155-MS.

Kvenvolden, K.A., 1988. Methane hydrate—A major reservoir of carbon in the shallow geosphere? Chem. Geol. 71 (1–3), 41–51. https://doi.org/10.1016/0009−2541(88)90104-0.

Lee, T., Lee, J.Y., Ahn, T., et al., 2021. Numerical simulation of gas hydrate production using the cyclic depressurization method in the Ulleung Basin of the Korea East Sea. Applied Sciences 11 (20), 9748. https://doi.org/10.3390/app11209748.

Lei, L., Santamarina, J.C., 2018. Laboratory strategies for hydrate formation in fine-grained sediments. J. Geophys. Res. Solid Earth 123 (4), 2583–2596. https://doi.org/10.1002/2017JB014624.

Li, B., Sun, Y., Jiang, S., et al., 2025. Production characteristics and sensitivity analysis on gas hydrate and shallow gas coexistence reservoirs. Focus on gas hydrate formation. Appl. Energy 386, 125572. https://doi.org/10.1016/j.apenergy.2025.125572.

Li, J., Ye, J., Qin, X., et al., 2018. The first offshore natural gas hydrate production test in South China Sea. China Geol. 1 (1), 5–16. https://doi.org/10.31035/cg2018003.

Li, S., Ding, S., Wu, D., et al., 2021a. Analysis of stratum subsidence induced by depressurization at an offshore hydrate-bearing sediment. Energy & Fuels 35 (2), 1381–1388. https://pubs.acs.org/doi/10.1021/acs.energyfuels.0c03833#Abstract.

Li, Y., Wang, L., Shen, S., et al., 2021b. Triaxial tests on water-saturated gas hydrate-bearing fine-grained samples of the South China Sea under different drainage conditions. Energy & Fuels 35 (5), 4118–4126. https://doi.org/10.1021/acs.energyfuels.1c00071.

Liu, S., Li, H., Wang, B., et al., 2022. Accelerating gas production of the depressurization-induced natural gas hydrate by electrical heating. J. Petrol. Sci. Eng. 208, 109735. https://doi.org/10.1016/j.petrol.2021.109735.

Makogon, Y.F., Holditch, S.A., Makogon, T.Y., 2007. Natural gas-hydrates—A potential energy source for the 21st Century. J. Petrol. Sci. Eng. 56 (1), 14–31. https://doi.org/10.1016/j.petrol.2005.10.009.

Mao, P., Wu, N., Ning, F., et al., 2023. Gas production from muddy hydrate reservoirs by a spiral multilateral well network: Effects of well deployment and production methods. Gas Sci. Eng. 118, 205087. https://doi.org/10.1016/j.jgsce.2023.205087.

Maslin, M., Owen, M., Day, S., et al., 2004. Linking continental-slope failures and climate change: testing the clathrate gun hypothesis. Geology 32 (1), 53–56. https://doi.org/10.1130/G20114.1.

Masui, A., Haneda, H., Ogata, Y., et al., 2007. Mechanical properties of sandy sediment containing marine gas hydrates in deep sea offshore Japan. In: Proceedings of Seventh ISOPE Ocean Mining Symposium. ISOPE-M-07-015.

Matsuda, H., Yamakawa, T., Sugai, Y., et al., 2016. Gas production from offshore methane hydrate layer and seabed subsidence by depressurization method. Engineering 8 (6), 353–364. https://doi.org/10.4236/eng.2016.86033.

Max, M.D., Johnson, A.H., 2018. Exploration and Production of Oceanic Natural Gas Hydrate: Critical Factors for Commercialization. Springer. https://doi.org/10.1007/978-030-00401-9.

Moridis, G.J., Collett, T.S., Dallimore, S.R., et al., 2004. Numerical studies of gas production from several CH_4 hydrate zones at the Mallik site, Mackenzie Delta, Canada. J. Petrol. Sci. Eng. 43 (3–4), 219–238. https://doi.org/10.1016/j.petrol.2004.02.015.

Qiu, Y., Wang, X., Wang, Z., et al., 2023. THMC fully coupled model of natural gas hydrate under damage effect and parameter sensitivity analysis. J. Mar. Sci. Eng. 11 (3), 612. https://doi.org/10.3390/jmse11030612.

Reid, R.C., Sherwood, T.K., Street, R.E., 1959. The properties of gases and liquids. Phys. Today 12 (4), 38–40. https://doi.org/10.1063/1.3060771.

Rutqvist, J., Moridis, G.J., Grover, T., et al., 2012. Coupled multiphase fluid flow and wellbore stability analysis associated with gas production from oceanic hydrate-bearing sediments. J. Petrol. Sci. Eng. 92, 65–81. https://doi.org/10.1016/j.petrol.2012.06.004.

Saffou, E., Gholami, R., Raza, A., et al., 2023. A one-way coupled geomechanical model for CO_2 storage in faulted depleted gas reservoirs. Gas Sci. Eng. 120, 205143. https://doi.org/10.1016/j.jgsce.2023.205143.

Shi, K., Wei, K., Jiang, Z., et al., 2024. Optimization of energy efficiency in gas production from hydrates assisted by geothermal energy enriched in the deep gas. Int. J. Heat Mass Tran. 234, 126122. https://doi.org/10.1016/j.ijheatmasstransfer.2024.126122.

Skarke, A., Ruppel, C., Kodis, M., et al., 2014. Widespread methane leakage from the sea floor on the northern US Atlantic margin. Nat. Geosci. 7 (9), 657–661. https://doi.org/10.1038/ngeo2232.

Sloan, E.D., Koh, C.A., 2007. Clathrate Hydrates of Natural Gases. CRC press. https://doi.org/10.1201/9781420008494.

Song, X., Nian, T., Mestdagh, T., et al., 2023. Long- and short-term dynamic stability of submarine slopes undergoing hydrate dissociation. Gas Sci. Eng. 111, 204934. https://doi.org/10.1016/j.jgsce.2023.204934.

Song, Y., Wang, X., Dong, Z., et al., 2024. Review and outlook on fracturing technology and mechanism of hydrate-bearing sediments. Energy & Fuels 38 (16), 14960–14981. https://doi.org/10.1021/acs.energyfuels.4c02524.

Sun, J., Ning, F., Zhang, L., et al., 2016. Numerical simulation on gas production from hydrate reservoir at the 1st offshore test site in the eastern Nankai Trough. J. Nat. Gas Sci. Eng. 30, 64–76. https://doi.org/10.1016/j.jngse.2016.01.036.

Sun, X., Luo, T., Wang, L., et al., 2019. Numerical simulation of gas recovery from a low-permeability hydrate reservoir by depressurization. Appl. Energy 250, 7–18. https://doi.org/10.1016/j.apenergy.2019.05.035.

Tiong, M., Peng, W., Liu, Q., et al., 2025. Natural gas hydrate exploitation: A comprehensive review of structural properties, technical progress and environmental challenges. Gas Sci. Eng. 144, 205769. https://doi.org/10.1016/j.jgsce.2025.205769.

Wan, T., Li, Z., Wen, M., et al., 2024. Numerical simulation of production behavior with different complex structure well types in class 1-type hydrate reservoir. J. Mar. Sci. Eng. 12 (3), 508. https://doi.org/10.3390/jmse12030508.

Wang, B., Chen, X., Xie, Y., et al., 2025. Hydrate formation in porous media with upward-migrating methane and its implications for the evolution of deep-sea cold seep ecosystems. Sci. Total Environ. 959, 178299. https://doi.org/10.1016/j.scitotenv.2024.178299.

Wang, B., Fan, Z., Wang, P., et al., 2018. Analysis of depressurization mode on gas recovery from methane hydrate deposits and the concomitant ice generation. Appl. Energy 227, 624–633. https://doi.org/10.1016/j.apenergy.2017.09.109.

Wang, F., Wang, Z., Zhang, D., et al., 2021. Statistical damage constitutive model based on self–consistent Eshelby method for natural gas hydrate sediments. Energy Sci. Eng. 9 (11), 2079–2098. https://doi.org/10.1002/ese3.968.

Wang, H., Wu, P., Li, Y., et al., 2023. Gas permeability variation during methane hydrate dissociation by depressurization in marine sediments. Energy 263, 125749. https://doi.org/10.1016/j.energy.2022.125749.

Wu, P., Li, Y., Liu, W., et al., 2020. Microstructure evolution of hydrate-bearing sands during thermal dissociation and ensued impacts on the mechanical and seepage characteristics. J. Geophys. Res. Solid Earth 125 (5), e2019JB019103. https://doi.org/10.1029/2019JB019103.

Wu, Z., Zhang, K., Wang, L., et al., 2022. Experimental study on the evolution of compressibility and gas permeability of sediments after hydrate decomposition under effective stress. Energy & Fuels 37 (2), 1033–1043. https://doi.org/10.1021/acs.energyfuels.2c03676.

Xue, M., Cheng, Y., Li, Y., et al., 2023. Numerical analysis on gas production and geomechanical responses of natural gas hydrate reservoirs. ACS Omega 8 (42), 39604–39615. https://doi.org/10.1021/acsomega.3c05484.

Yamamoto, K., Terao, Y., Fujii, T., et al., 2014. Operational overview of the first offshore production test of methane hydrates in the Eastern Nankai Trough. In: Proceedings of Offshore Technology Conference. https://doi.org/10.4043/25243-MS.

Yamamoto, K., Wang, X.-X., Tamaki, M., et al., 2019. The second offshore production of methane hydrate in the Nankai Trough and gas production behavior from a heterogeneous methane hydrate reservoir. RSC Adv. 9 (45), 25987–26013. https://doi.org/10.1039/c9ra00755e.

Yang, R., Wang, F., Rao, Z., et al., 2024. Advancing sustainable energy solutions: Innovations in clean energy applications and conventional energy efficiency upgrade. Energies 17 (10), 2441. https://doi.org/10.3390/en17102441.

Yang, Y., He, Y., Zheng, Q., 2017. An analysis of the key safety technologies for natural gas hydrate exploitation. Adv. Geo-Energy Res. 1 (2), 100–104. https://doi.org/10.26804/ager.2017.02.05.

Yao, Y., Niu, M., Sun, Y., et al., 2024. Significance of well placement and degree of hydrate reserve recovery for synergistic CH_4 recovery and CO_2 storage in marine heterogeneous hydrate-bearing sediments. Geoenergy Sci. Eng. 242, 213290. https://doi.org/10.1016/j.geoen.2024.213290.

Ye, H., Chen, D., Yao, Y., et al., 2024. Exploration of production capacity-geomechanical evaluation and CO_2 reinjection repair strategy in natural gas hydrate production by multilateral horizontal wells. Energy 296, 131097. https://doi.org/10.1016/j.energy.2024.131097.

Ye, H., Chen, J., Yao, Y., et al., 2025a. Gas recovery from low-permeability muddy silt gas hydrate reservoirs by depressurization coupled with hot water injection: Impact of hydro-lock effect. Energy 316, 134413. https://doi.org/10.1016/j.energy.2025.134413.

Ye, H., Li, J., Yao, Y., et al., 2026. Distinct gas production characteristics from laboratory-synthesized Class I, II, and III hydrate reservoirs: A novel thermally-segmented rotatable approach. Int. J. Min. Sci. Technol. 36 (3), 651–665. https://doi.org/10.1016/j.ijmst.2025.12.016.

Ye, J., Qin, X., Xie, W., et al., 2020. The second natural gas hydrate production test in the South China Sea. China Geol. 3 (2), 197–209. https://doi.org/10.31035/cg2020043.

Ye, H., Yao, Y., Chen, D., et al., 2025b. Hydrate-based CO_2 sequestration in post-exploitation natural gas hydrate reservoir: A numerical method considering mixed hydrate. Energy 336, 138406. https://doi.org/10.1016/j.energy.2025.138406.

Yin, F., Gao, Y., Chen, Y., et al., 2022. Numerical investigation on the long-term production behavior of horizontal well at the gas hydrate production site in South China Sea. Appl. Energy 311, 118603. https://doi.org/10.1016/j.apenergy.2022.118603.

Yoneda, J., Masui, A., Konno, Y., et al., 2015. Mechanical properties of hydrate-bearing turbidite reservoir in the first gas production test site of the Eastern Nankai Trough. Mar. Petrol. Geol. 66, 471–486. https://doi.org/10.1016/j.marpetgeo.2015.02.029.

Yoneda, J., Takiguchi, A., Ishibashi, T., et al., 2018. Mechanical response of reservoir and well completion of the first offshore methane-hydrate production test at the Eastern Nankai Trough: a coupled thermo-hydromechanical analysis. SPE J. 24 (2), 531–546. https://doi.org/10.2118/191145-PA.

Yuan, W., Feng, J.-C., Li, B., et al., 2025. Assessing the prospect of long-term exploitation of Class 1 hydrate deposit with horizontal well in the South China Sea from energy, environmental, and economic perspectives. Appl. Energy 400, 126552. https://doi.org/10.1016/j.apenergy.2025.126552.

Zhang, H., Nian, T., Song, X., et al., 2025. Effect of wellhead depressurization on the stability of submarine hydrate-bearing reservoir using THMC coupling. Energy 320, 134961. https://doi.org/10.1016/j.energy.2025.134961.

Zhang, X.H., Lu, X.B., Shi, Y.H., et al., 2015. Study on the mechanical properties of hydrate-bearing silty clay. Mar. Petrol. Geol. 67, 72–80. https://doi.org/10.1016/j.marpetgeo.2015.04.019.

Zhu, H., Xu, T., Yuan, Y., et al., 2020. Numerical investigation of the natural gas hydrate production tests in the Nankai Trough by incorporating sand migration. Appl. Energy 275, 115384. https://doi.org/10.1016/j.apenergy.2020.115384.